Applied Mathematical Modelling 40 (2016) 4480–4504

Contents lists available at ScienceDirect

Applied Mathematical Modelling

journal homepage: www.elsevier.com/locate/apm

# Coupled mechanical and fluid flow analysis in fractured saturated porous media using the XFEM

Mariela Luege [a,*], Javier Lucero [a], Celeste Torrijos [b], Antonio Orlando [a]

[a] CONICET, Instituto de Estructuras, Universidad Nacional de Tucumán, San Miguel de Tucumán, Tucumán, Argentina
[b] CONICET, LEMIT, La Plata, Buenos Aires, Argentina

ARTICLE INFO

*Article history:*
Received 2 September 2015
Revised 4 November 2015
Accepted 19 November 2015
Available online 2 December 2015

*Keywords:*
Fractured porous media
Biot–Coussy model
Singular integral equation
Extended Finite Element Method

ABSTRACT

In this paper, we study the fluid flow in a deformable porous linear elastic media with a single crack $\Gamma$. Fluid exchange between the crack and the surrounding porous media is taken into account through the definition of appropriate boundary conditions on $\Gamma$ obtained by applying an averaging process of the Darcy flow within the crack. Two models are considered and compared: a semianalytical one which solves the general potential solution of the singular integral equation modelling the steady state flow in an infinite porous media with one linear crack, obtained by applying the complex potential method, and a numerical one based on the Extended Finite Element Method (XFEM) of the governing equations. The XFEM we apply employs the standard enriched basis functions represented by the Heaviside function on $\Gamma$ to describe the discontinuity jump of the displacement field across the crack, the distance function to $\Gamma$ to describe the non differentiability of the pressure field across $\Gamma$ and the singular functions describing the $\sqrt{r}$-singularity at the crack tip of the stress and pressure field, where $r$ is the distance to the crack tip. The semianalytical model is used to verify the application of the XFEM. We include then the coupling with the mechanical response of the body, which is analyzed by using only the XFEM. Several numerical experiments are then carried out which illustrate the variation of the hydro-mechanical quantities around the crack and within the crack.



## 1. Introduction

The analysis of the hydro-mechanical behaviour of fully saturated fractured porous media is significant in many engineering applications, such as flow transport in geologic media, hydraulic fracturing for petroleum engineering and mining industry, permeability analysis for damage estimation, environmental engineering, just to mention few. Given its relevance to the applications, this problem has received much attention in the scientific community and has been analysed from the experimental, analytical and numerical point of view.

The experimental studies carried out on the steady-state flow in fractured rocks, geological formations or concrete under given far field conditions, provide information on the effective permeability of the medium, the connected voids and the interconnection with macro and micro cracks of the material under study. Experiments on water permeability and its variation with crack opening on saturated concrete specimens are reported in [1], where splitting tensile tests (Brazilian test) have been used for concrete fracturing tests. Further experimental results on permeability of damaged concrete can be found in [2], where the

* Corresponding author. Tel.: +54 3814259246.
*E-mail address:* mluege@herrera.unt.edu.ar, mluege@yahoo.com (M. Luege).

http://dx.doi.org/10.1016/j.apm.2015.11.032
S0307-904X(15)00747-7/

concrete specimens deteriorate as a result of the exposition to high temperature conditions and of alkali silica reactions. The final aim of these experiments is to quantify the level of deterioration of a material from its transport properties. Since the occurrence of damage modifies the elastic properties and permeability of the material, the importance of studying cracking processes and its influence in fluid flow is of major interest for the durability analysis of structures.

Exact analytical solutions have been developed mainly for some simplified geometries. For the case of steady state flow, the pressure is solution of the Laplace equation which is uncoupled from the equations of linear elasticity. As a result, the techniques of solutions that have been applied are the classical one for finding harmonic functions in a domain with no-Lipschitz boundary. A frequently adopted method of solution is the one based on a complex potential representation of the solution. This for instance has been employed in [3] where an extension of the Muskhelishvili formalism of classical elasticity [4] is developed for stress diffusion problems. Another instance of application of this method is given in [5], where the authors consider the cracks as singularity lines of the complex potentials representing the pore pressure solution and propose a corresponding form of such potentials. The enforcement then of the boundary condition given in terms of known discharges along the non intersecting cracks leads to a singular integral equation which is solved by applying a Gauss–Chebyshev numerical integration scheme for singular integral equations [6]. This procedure has then been extended in [7,8] for more general cracks configurations and crack boundary conditions, considering the case of intersecting cracks in an infinite anisotropic material and of cracks with a Poiseuille type conductivity.

For more complex geometries and crack configurations, it becomes necessary to resort to numerical methods that are capable to describe the different type of singularities that can experience the solution field variables. For the equations of poroelasticity in a slit domain, if we denote by $\Gamma$ the slit contained in $\Omega$, the solutions of the field equations, expressing the momentum and mass balance, are generally expected to be no regular in $\Omega$ with the lack of regularity due to discontinuity jumps across $\Gamma$ and singular behaviour at the crack tips [9]. In this case, the application of standard conforming $H^1$-finite element methods is known to perform quite poorly because of the singularity in the stress field, and the inherent inability to model fields with discontinuity jumps which are not $H^1$-functions. A standard approach in FE practice would thus be the use of a mesh with edges aligned to the crack and the splitting of nodes along the crack to model the discontinuity jump (a stratagem to model piecewise $H^1$-functions), and the design of very fine meshes around the crack tip. By these approaches, however, a-priori knowledge of the location of the discontinuity jump is required which must be aligned with the mesh edges. The XFEM (extended finite element method) introduced in the works of [10,11], on the other hand, has the ability to model the effects produced by the presence of geometric singularities, such as cracks, cavities, material heterogeneity, independently of the mesh. This technique relies on a suitable enrichment of the standard conforming finite element space by so called enrichment functions that are meant to account for the singularity of the solution which could not be otherwise described by the standard conforming finite element shape functions. The method exploits the partition of unity property of the finite elements [12,13], that is, the sum of the shape functions must equal to the unity, which in turn permits the shape functions to reproduce the constant function, which is a crucial condition for the convergence of the method.

Applications of the XFEM to porous media are given in [14–17] where the emphasis is placed mainly on the modeling of the fluid flow and of the fluid exchange between the cavity and the surrounding porous media which is realised by means of an averaging process of the Stokes equations in the cavity, whereas [18,19] address implementation issues of the application of the method and extend it to the modelling of hydraulic fracturing using a cohesive crack model. The literature on the applications of the XFEM to hydraulic fracturing, i.e. the production of cracks by the injection of fluid into a linear elastic brittle material, is quite abundant [20–24]. In these works, the focus is mainly on the evaluation of the order of the pole of the pore pressure which is not of the type $\sqrt{r}$, with $r$ the distance to the crack tip, and on how to choose consistently the enrichment shape functions. We conclude, finally, by mentioning also the work [25] for an instance of application of the XFEM to capture the effects of an arbitrary interior interface in the two-phase immiscible flow problem.

In this paper we present a numerical model of the fluid flow in a deformable porous linear elastic fractured medium which is built upon the XFEM and a reduced model of the fluid flow in the cracks. The XFEM is used to model the deformation of the fractured porous medium and the singularities of the pressure gradient and velocity fields with meshes that are not aligned with the crack interface, whereas the reduced model of the fluid flow is used to account for the reduced dimensionality of the fracture geometry and of the type of flow therein, thus providing a considerable simplification of the governing equations within the crack. We then also compare the performance of our numerical model to a semianalytical solution for the case of steady-state flow. The governing equations are obtained in Section 2 by applying the theory of linear poroelasticity of Biot–Coussy [26]. Both the domain occupied by the porous medium and the cracks are considered fully saturated. For the description of the coupled hydromechanical behaviour of fracture media with cracks modelled individually, different approaches can be followed according to the scale of description one adopts. A global simulation of the hydromechanical behaviour of the porous media and the cracks, considered with their dimensionality, would result in a heavy computational model for the excessive mesh refining needed within the crack and would be therefore very expensive, especially in the case of thin cracks which are the type of cracks we are considering in this paper. In this case, therefore, it results more convenient to account of the reduced dimensionality of the fracture geometry and derive reduced models of flow within the crack [15,27–29]. According to this approach, which is the one we are interested in, the fractures are reduced to sharp interfaces $\Gamma$ which are treated as internal material boundaries of the porous medium endowed with a hydromechanical behaviour. The setting of the interface conditions on $\Gamma$ is, however, a delicate issue which is currently still object of investigation [30–35,43,44]. In this paper, we will account for the influence of the flow exchange between the crack and the neighbouring porous media through an accurate modelling of the flow along $\Gamma$. At variance of [15] where in deriving the interface conditions the cavity is considered filled with a Stokes flow, in Section 2.6, we will assume

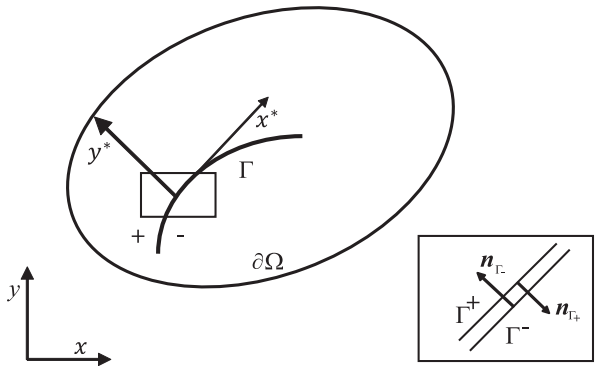


**Fig. 1.** Infinitesimal saturated porous volume with a single discontinuity and definition of the sides $\Gamma^+$ and $\Gamma^-$.

that the crack is filled with porous media and determine the conditions on the interface $\Gamma$ by averaging the Darcy flow within the crack [27,29]. We will then proceed in Section 3 to describe the fully coupled discrete model. This is obtained by applying the XFEM with the standard enriched basis functions as introduced in [11,23] for the space discretisation of the governing equations. The enriched basis functions are represented by: (*i*) the Heaviside function to describe the discontinuity jump of the displacement field across the crack; (*ii*) the signed distance to describe the non differentiability of the pressure field across $\Gamma$; and (*iii*) singular functions describing the $\sqrt{r}$-singularity at the crack tip of the stress and pressure field, where $r$ is the distance to the crack tip. Since the terms that describe the interaction between the flow within the crack and the deformation of the surrounding porous media enter only through integrals defined over $\Gamma$, with the interface $\Gamma$ being fixed, we will use also an XFEM type interpolation of the field variables when evaluating such integrals. The application of XFEM to this problem has similarities to the immerse interface method and its variants discussed in [36] where the effects of the interface are taken into account by means of *ad-hoc* modifications of the finite difference schemes at the grid points near the interface [37]. For the time discretisation of the resulting system of ordinary differential equations, we will then use the backward Euler method. To verify the resulting numerical model, we will consider in Section 4 the special case of steady-state flow. Under this hypothesis, the linear poroelastic equations uncouple into the Laplace equation for the pore pressure and the linear elastic equation for the effective stress. We solve therefore the Laplace equation by applying the complex potential method. The use of this method and the enforcement of the boundary conditions on $\Gamma$, given either by a prescribed pressure or by a Poiseuille conductivity type, transform the original Laplace equation into a singular integral equation of the first kind, which we solve numerically using the collocation method on Chebyshev nodes and Lobatto–Chebyshev quadratures [6]. The final section is devoted to numerical experiments where we compare the two numerical models for the special case of steady-state flow; we discuss then a permeability test where the XFEM numerical solution is compared to available experimental results and finally we give an example where we analyse the fully coupled poroelastic problem in a fractured domain.

## 2. Governing equations of a fractured porous media

The saturated porous medium is next modelled as a two phase system: a solid deformable porous phase and a fluid phase that fills the void spaces. The governing equations are then given by the balance equations of linear momentum and mass and the constitutive equations of each phase. This section is devoted to derive briefly the governing equations of poroelasticity [38,39] and to model the fluid flow exchange across the cracks. This will be carried out following a two-scale approach as described in [14–16,40].

### 2.1. Model problem and notation

We assume that the domain $\Omega \subset \mathbb{R}^N$ occupied by the porous media contains some cracks in its inside, i.e. $\Gamma \subset \Omega$ with $\Gamma$ being a manifold of dimension less than $N$. For instance, if $N = 3$, $\Gamma$ will be either a surface or a line. In this work, we consider $N = 2$, and $\Gamma$ will represent lines contained in $\Omega$. The sets of the cracks is denoted by $\Gamma$. Each component of $\Gamma$ is described in terms of a smooth function $\boldsymbol{z} = \boldsymbol{z}(x^*)$ which represents the parametric equation of the curve as a function of the curvilinear coordinate $x^*$ along the crack (see Fig. 1).

In this work, we consider non-intersecting cracks. Each crack has an orientation defined by the normal $\boldsymbol{n}_\Gamma$ to the curve at $\boldsymbol{z} \in \Gamma$. The choice of $\boldsymbol{n}_\Gamma$ along with the tangent unit vector $\boldsymbol{t}_\Gamma$ determines a positive face of $\Gamma$ which we denote by $\Gamma^+$ and a negative face of $\Gamma$ which we denote by $\Gamma^-$. The definition of these two sides of $\Gamma$ in relation to $\boldsymbol{n}_\Gamma$ becomes relevant when we need to apply the divergence theorem. The curve $\Gamma$ does idealise a crack. In the definition of the boundary conditions on $\Gamma$, we will need to consider $\Gamma$ endowed with a structure, that is, $\Gamma$ will be seen as the boundary of a cavity $\Omega_c$ which in this treatment is assumed to have $L \gg 2h$, where $h$ is the crack width and $L$ is the characteristic crack length. The assumption $L \gg 2h$ justifies the averaging process in Section 2.6 of the fields equations within the cavity.

### 2.2. Thermodynamic framework and constitutive equations

For the derivation of the constitutive equations, we start from the Clausius–Duhem inequality which, for a deformable porous continua, takes the form [39]

$$\Phi = \Phi_s + \Phi_f + \Phi_{th} \geq 0,$$

where $\Phi$ represents the overall dissipation, whereas $\Phi_s$ and $\Phi_f$ are the solid and fluid sources of dissipation, respectively. The thermal dissipation $\Phi_{th}$ is assumed to be equal to zero given that in this paper, we will consider only isothermal processes. Next let us denote by $\boldsymbol{\sigma}$ the total stress tensor, by $\boldsymbol{u}$ the displacement of the solid phase, by $\boldsymbol{\varepsilon}$ the corresponding strain tensor given by $\boldsymbol{\varepsilon} = (\nabla \boldsymbol{u} + \nabla \boldsymbol{u}^T)/2$ where $\nabla$ is the gradient operator so that for $\boldsymbol{u} \in \mathbb{R}^N$, $(\nabla \boldsymbol{u})_{ij} = u_{i,j}$, $i, j = 1, \ldots, N$ is the partial derivative of the component $u_i$ of the field $\boldsymbol{u}$ with respect to the coordinate variable $x_j$, whereas the superscript $T$ denotes the transpose operation. Under the assumption of small deformations, the solid matrix dissipation $\Phi_s$ is given by

$$\Phi_s = \boldsymbol{\sigma} : \frac{d\boldsymbol{\varepsilon}}{dt} - \phi \frac{dp}{dt} - \frac{dG_s}{dt}, \tag{2.1}$$

where $\phi$ denotes the Lagrangian porosity and $G_s = G_s(\boldsymbol{e}, p)$ the free Gibbs energy with $p$ the pore pressure. The term $\phi dp/dt$ takes into account the dissipation associated with the pore pressure acting on the matrix porous walls. The Lagrangian porosity $\phi$ is related to the spatial porosity $n$ by the relation $\phi d\Omega_0 = n d\Omega$ which for small deformations reduces to $\phi = Jn \approx (1 + \epsilon)n$, with $J$ the Jacobian determinant of the strain tensor, i.e. $J = \det \boldsymbol{\varepsilon}$ where det is the determinant operator. To obtain the equations of linear isotropic poroelasticity, let tr denote the trace operator and $\boldsymbol{1}$ the identity second order tensor, then we consider for the quadratic Gibbs free energy $G_s$ the following function of the first ($\epsilon = \mathrm{tr}\boldsymbol{\varepsilon}$) and the second ($\boldsymbol{e}$: $\boldsymbol{e}$) strain invariant with $\boldsymbol{e} = \boldsymbol{\varepsilon} - \frac{1}{3}\epsilon \boldsymbol{1}$

$$G_s(\varepsilon, \boldsymbol{e}, p) = \frac{1}{2} K \varepsilon^2 - bp\varepsilon - \frac{1}{2}\frac{p^2}{N} + G\boldsymbol{e} : \boldsymbol{e}, \tag{2.2}$$

where $G$ and $K$ denote the shear and drained volumetric elastic modulus of the porous media, respectively; $b = 1 - K/K_s \leq 1$ is the Biot's coefficient with $K_s$ the bulk modulus of the solid grains; $1/N = (b - \phi_0)/K_s$ is the Biot's modulus and $\phi_0$ is the initial porosity. By replacing (2.2) into (2.1), poroelasticity is then defined by the condition that $\Phi_s = 0$ for all the admissible processes, which yields

$$\boldsymbol{\sigma} = 2G\boldsymbol{e} + (K\epsilon - bp)\boldsymbol{1}\,; \quad \phi = b\epsilon - \frac{p}{N}. \tag{2.3}$$

The dissipation associated with the fluid motion with respect to the solid matrix is given by

$$\Phi_f = -\nabla p \cdot n(\boldsymbol{v}_f - \boldsymbol{v}_s). \tag{2.4}$$

where $\boldsymbol{v}_s = d\boldsymbol{u}/dt$ is the velocity of the solid grains and $\boldsymbol{v}_f$ the fluid velocity inside the porous space. If we consider the Darcy's law for the fluid phase, the constitutive equation is given by

$$n(\boldsymbol{v}_f - \boldsymbol{v}_s) = -k_f \nabla p, \tag{2.5}$$

with $k_f$ the permeability constant and $\nabla p = \partial p/\partial \boldsymbol{x}$. Eq. (2.5) ensures that the fluid dissipation is non negative.

### 2.3. Balance equations

If we assume that the deformation of the solid is much slower than the flow rate, we can consider quasistatic conditions and neglect the inertial terms. In this case, and for negligible body forces, the momentum conservation equation is given by

$$\nabla \cdot \boldsymbol{\sigma} = \boldsymbol{0} \quad \text{in } \Omega \setminus \Gamma. \tag{2.6}$$

Let us denote by $\rho_f$ the fluid density. Under the assumption of incompressible solid grains, the mass conservation equations for the fluid and solid phase yield

$$\frac{n}{\rho_f}\frac{\partial \rho_f}{\partial t} + \nabla \cdot \boldsymbol{v}_s + \nabla \cdot n(\boldsymbol{v}_f - \boldsymbol{v}_s) = 0 \quad \text{in } \Omega \setminus \Gamma. \tag{2.7}$$

Eq. (2.7) can be conveniently rewritten in terms of the pore pressure $p$ by invoking the state equation that describes the ability of the water to change mass due to changes in the hydrostatic pressure. By assuming the following relation [41]

$$\frac{1}{\rho_f}\frac{\partial \rho_f}{\partial t} = \frac{1}{K_f}\frac{\partial p}{\partial t}, \tag{2.8}$$

with $K_f$ the bulk modulus of the fluid, and replaced into (2.7) yields

$$\frac{n}{K_f}\frac{\partial p}{\partial t} + \nabla \cdot \boldsymbol{v}_s + \nabla \cdot n(\boldsymbol{v}_f - \boldsymbol{v}_s) = 0 \quad \text{in } \Omega \setminus \Gamma. \tag{2.9}$$

### 2.4. Boundary conditions and summary of the governing equations

The balance equations (2.6) and (2.9) along with the constitutive equations (2.3) and (2.5) form a close system of equations in the unknowns $\boldsymbol{u}$, $\boldsymbol{v}_f$, $p$ and $n$, and $\boldsymbol{v}_s = \frac{d\boldsymbol{u}}{dt}$. Such equations must, however, be supplemented by initial and boundary conditions. While the setting of the initial conditions does not require particular observations, some considerations are deemed necessary in the choice of the boundary conditions. Given the nature of the problem, we will need to consider two different sets of boundary conditions, one corresponding to the flow and the other one corresponding to the deformation. For each of them we can have Dirichlet type boundary conditions and Neumann type boundary conditions. Since the solutions are sought within the domain $\Omega\backslash\Gamma$, its boundary $\partial(\Omega\backslash\Gamma)$ will be given by the union of the boundary $\partial\Omega$ of $\Omega$ and of the set of cracks $\Gamma$. The boundary $\partial\Omega$ is correspondingly partitioned into $\partial\Omega = \partial_v\Omega \cup \partial_p\Omega$ for the flow type boundary conditions and into $\partial\Omega = \partial_u\Omega \cup \partial_t\Omega$ for the deformation type boundary conditions. In this paper, we will consider therefore the following deformation type boundary conditions

$$\boldsymbol{u} = \bar{\boldsymbol{u}} \quad \text{on } \partial_u\Omega \quad \boldsymbol{\sigma}\boldsymbol{n} = \bar{\boldsymbol{t}} \quad \text{on } \partial_t\Omega, \tag{2.10}$$

where $\boldsymbol{n}$ is the outward normal to $\partial\Omega$, $\bar{\boldsymbol{t}}$ is the prescribed external traction and $\bar{\boldsymbol{u}}$ the prescribed displacement at the boundary, and the following flow type boundary conditions:

$$p = \bar{p} \quad \text{on } \partial_p\Omega \quad n(\boldsymbol{v}_f - \boldsymbol{v}_s)\cdot\boldsymbol{n} = \bar{v} \quad \text{on } \partial_v\Omega, \tag{2.11}$$

where $\bar{v}$ is the prescribed outflow of pore fluid and $\bar{p}$ the prescribed pressure. A similar partition of the boundary conditions could be done in principle also for $\Gamma$. However, on $\Gamma$ we will consider only Neumann type boundary conditions for the deformation and for the flow. The definition of these conditions is essential because they determine the coupling between the flow in the porous media around the crack and the flow within the crack. For the deformation type Neumann boundary conditions, we assume that the tractions are the same on each side of $\Gamma$ and these tractions are imposed by the fluid pressure inside $\Gamma$, that is

$$\boldsymbol{\sigma}\boldsymbol{n}_\Gamma = p\boldsymbol{n}_\Gamma \quad \text{on } \Gamma, \tag{2.12}$$

where $\boldsymbol{n}_\Gamma$ is the normal to $\Gamma$. By this condition, we are basically enforcing that the pore pressure field is continuous across $\Gamma$. On the other hand, it is natural to assume that the velocity field of the fluid and solid phase is discontinuous across $\Gamma$. If we therefore introduce the notation $[\![\boldsymbol{w}]\!] := \boldsymbol{w}|_{\Gamma^+} - \boldsymbol{w}_f|_{\Gamma^-}$ to denote the jump of a variable field $\boldsymbol{w}$ across $\Gamma$, the flow type Neumann boundary conditions will be given as follows:

$$n[\![\boldsymbol{v}_f - \boldsymbol{v}_s]\!]\cdot\boldsymbol{n}_\Gamma = q \quad \text{on } \Gamma, \tag{2.13}$$

where $q$ represents a flux across $\Gamma$. In the applications we can consider the case where such flux is prescribed or the case where such flux depends on the flow which occurs within the cracks $\Gamma$. An instance of the latter is given, for instance, if we assume a laminar flow through parallel planar plates to represent the fracture surface. Such condition is next referred to as Poiseuille flow inside the crack. In this case, we can set

$$q = -k_d\nabla p\cdot\boldsymbol{t}_\Gamma \quad \text{on } \Gamma, \tag{2.14}$$

where $\boldsymbol{t}_\Gamma$ is the tangent vector to $\Gamma$ and $k_d$ is the hydraulic conductivity, given by [42] as $k_d = (2h)^3/(12f\mu)$, where $2h$ is the crack width, $\mu$ is the fluid viscosity and $f$ is a coefficient that depends on the crack surface roughness and accounts for the deviations from the ideal conditions of laminar flow in an open fracture modelled by the cubic law. The values of $f$ depend on the material by which the porous media is made of, and are obtained from experimental observations following, for instance, the laboratory procedure described in [42, page. 1018]. The case of void crack can also be described by this equation and would correspond to $k_d \to \infty$ giving constant pressure along the crack. By combining (2.13) and (2.14), we obtain therefore the following boundary condition on $\Gamma$:

$$n[\![\boldsymbol{v}_f - \boldsymbol{v}_s]\!]\cdot\boldsymbol{n}_\Gamma = -k_d\nabla p\cdot\boldsymbol{t}_\Gamma \quad \text{on } \Gamma. \tag{2.15}$$

According to this condition, it is assumed therefore that the fluid that enters the cavity diffuses tangentially within the cavity. As a result, the fluid flow normal to the crack is discontinuous, and consequently is also $\nabla p$. Across $\Gamma$ the pore pressure $p$ is continuous but it is not differentiable. We also note that (2.15) is a special case of oblique derivative boundary condition.

It is possible also to give more refined models of boundary conditions on $\Gamma$, for instance, by relating $q$ to the behaviour of the porous media within the crack. For this aspect, we refer to Section 2.6.

The complete set of the strong form of the governing equations along with the boundary conditions is given, for convenience, in Box 1.

### 2.5. Weak form of the governing equations

Starting from the strong form of the equations, we derive the corresponding weak forms. We assume as primary variables the fields $\boldsymbol{u}$ and $p$ and recall that $\boldsymbol{u}$ can experience discontinuities across $\Gamma$ whereas $p$ is continuous across $\Gamma$ but it is not differentiable. As test function for the momentum equations we therefore take functions $\delta\boldsymbol{u} = \boldsymbol{0}$ on $\partial_u\Omega$ and discontinuous across $\Gamma$, whereas

$$\nabla \cdot \boldsymbol{\sigma} = \mathbf{0} \quad \text{in } \Omega \setminus \Gamma\,;$$

$$\frac{n}{K_f}\frac{\partial p}{\partial t} + \nabla \cdot \boldsymbol{v}_s + \nabla \cdot n(\boldsymbol{v}_f - \boldsymbol{v}_s) = 0 \quad \text{in } \Omega \setminus \Gamma\,;$$

$$\boldsymbol{\sigma} = 2G\boldsymbol{e} + (K\epsilon - bp)\mathbf{1}\,;$$

$$\phi = b\epsilon - \frac{p}{N}\,;$$

$$n(\boldsymbol{v}_f - \boldsymbol{v}_s) = -k_f \nabla p\,;$$

$$\boldsymbol{u} = \bar{\boldsymbol{u}} \quad \text{on } \partial_u\Omega \qquad \boldsymbol{\sigma}\boldsymbol{n} = \bar{\boldsymbol{t}} \quad \text{on } \partial_t\Omega\,;$$

$$p = \bar{p} \quad \text{on } \partial_p\Omega \qquad n(\boldsymbol{v}_f - \boldsymbol{v}_s)\cdot\boldsymbol{n} = \bar{v} \quad \text{on } \partial_v\Omega\,;$$

$$\boldsymbol{\sigma}\boldsymbol{n}_\Gamma = p\boldsymbol{n}_\Gamma \quad \text{on } \Gamma \qquad n[\![\boldsymbol{v}_f - \boldsymbol{v}_s]\!]\cdot\boldsymbol{n}_\Gamma = -k_d \nabla p \cdot \boldsymbol{t}_\Gamma \quad \text{on } \Gamma\,;$$

$$\boldsymbol{u}(t=0) = \boldsymbol{u}_0 \quad \text{in } \Omega \setminus \Gamma \qquad p(t=0) = p_0 \quad \text{in } \Omega \setminus \Gamma\,.$$

**Box 1.** Strong Form of the Governing Equations.

for the mass balance equation we take scalar functions $\delta p = 0$ on $\partial_p\Omega$ and continuous across $\Gamma$. With this choice of the test functions, we have

$$\int_\Omega \boldsymbol{\sigma} : \nabla(\delta\boldsymbol{u})\,\mathrm{d}\boldsymbol{x} - \int_{\partial_t\Omega} \bar{\boldsymbol{t}}\cdot\delta\boldsymbol{u}\,\mathrm{d}s - \int_\Gamma p\boldsymbol{n}_\Gamma \cdot [\![\delta\boldsymbol{u}]\!]\,\mathrm{d}s = 0$$
$$\int_\Omega \frac{n}{K_f}\frac{\partial p}{\partial t}\delta p\,\mathrm{d}\boldsymbol{x} + \int_\Omega \nabla\cdot\boldsymbol{v}_s\,\delta p\,\mathrm{d}\boldsymbol{x} + \int_{\Omega\setminus\Gamma} \nabla\cdot n(\boldsymbol{v}_f - \boldsymbol{v}_s)\,\delta p\,\mathrm{d}\boldsymbol{x} = 0. \tag{2.16}$$

The weak form of the mass equation is convenient to re-write by applying the divergence theorem on the last term as follows:

$$\int_{\Omega\setminus\Gamma} \nabla\cdot n(\boldsymbol{v}_f - \boldsymbol{v}_s)\,\delta p\,\mathrm{d}\boldsymbol{x} = -\int_{\Omega\setminus\Gamma} n(\boldsymbol{v}_f - \boldsymbol{v}_s)\cdot\nabla\delta p\,\mathrm{d}\boldsymbol{x} + \int_{\partial_v\Omega} n(\boldsymbol{v}_f - \boldsymbol{v}_s)\cdot\boldsymbol{n}\,\delta p\,\mathrm{d}s + \int_\Gamma [\![n(\boldsymbol{v}_f - \boldsymbol{v}_s)]\!]\cdot\boldsymbol{n}_\Gamma\delta p\,\mathrm{d}s, \tag{2.17}$$

so that the flow type boundary conditions (2.11) and (2.13) can be enforced in the integral over $\partial_v\Omega$ and $\Gamma$, respectively.

### 2.6. Averaged flow equation within the cavity and reduction to the boundary

A more refined model which accounts for the flow within the crack can be obtained by relating the flow $q$ across $\Gamma$ originating in the porous media to the flow within the crack itself. In this model $\Gamma$ is seen as an idealised line to which we reduce the flow within the crack by averaging the flow equations over the width of the cavity. To realise this averaging process, we consider $\Gamma$ as the boundary of a cavity domain $\Omega_c$ with a characteristic length $L \gg h$, with $2h$ the crack width, and make some assumptions on the variation of the field variables within the cavity. Starting from the weak form of the mass balance within the domain $\Omega_c$,

$$\int_{\Omega_c} \frac{n}{K_f}\frac{\partial p}{\partial t}\delta p\,\mathrm{d}\boldsymbol{x} + \int_{\Omega_c} \nabla\cdot\boldsymbol{v}_s\,\delta p\,\mathrm{d}\boldsymbol{x} + \int_{\Omega_c} \nabla\cdot n(\boldsymbol{v}_f - \boldsymbol{v}_s)\,\delta p\,\mathrm{d}\boldsymbol{x} = 0, \tag{2.18}$$

after applying the divergence theorem to the last term in (2.18), we can solve the resulting equation with respect to $\int_\Gamma [\![n(\boldsymbol{v}_f - \boldsymbol{v}_s)]\!]\cdot\boldsymbol{n}_\Gamma\,\delta p\,\mathrm{d}s$ as follows:

$$\int_\Gamma [\![n(\boldsymbol{v}_f - \boldsymbol{v}_s)]\!]\cdot\boldsymbol{n}_\Gamma\,\delta p\,\mathrm{d}s = \int_{\Omega_c} \frac{n}{K_f}\frac{\partial p}{\partial t}\delta p\,\mathrm{d}\boldsymbol{x} + \int_{\Omega_c} \nabla\cdot\boldsymbol{v}_s\,\delta p\,\mathrm{d}\boldsymbol{x} + \int_{\Omega_c} n(\boldsymbol{v}_f - \boldsymbol{v}_s)\cdot\nabla\delta p\,\mathrm{d}\boldsymbol{x}. \tag{2.19}$$

The term $\int_\Gamma n(\boldsymbol{v}_f - \boldsymbol{v}_s)\cdot\boldsymbol{n}_\Gamma\,\nabla\delta p\,\mathrm{d}s$ provides the coupling between the flow within the crack and the flow within the porous media.

Let $\Omega_c = ]-h, h[\times\Gamma$ and denote by $(x^*, y^*)$ a curvilinear coordinate system with $x^*$ a curvilinear coordinate along $\Gamma$ and $y^*$ the coordinate along the normal direction to $\Gamma$. We represent $\Omega_c$ within this reference system. Denote then by $(v_{sx^*}, v_{sy^*})$ the components of $\boldsymbol{v}_s$ in such reference system. We assume that $p(\boldsymbol{x})$ is constant across the crack width, i.e. $\partial p/\partial y^* = 0$ and that $v_{sx^*}$ varies linearly along the coordinate axis $y^*$. Under these assumptions, we can then integrate along the crack thickness and have

$$\int_{\Omega_c} \frac{n}{K_f}\frac{\partial p}{\partial t}\delta p\,\mathrm{d}\boldsymbol{x} = \int_\Gamma\int_{-h}^{h} \frac{n}{K_f}\frac{\partial p}{\partial t}\delta p\,\mathrm{d}x^*\,\mathrm{d}y^* = \int_\Gamma \frac{2hn}{K_f}\frac{\partial p}{\partial t}\delta p\,\mathrm{d}x^*\,;$$
$$\int_{\Omega_c} \nabla\cdot\boldsymbol{v}_s\,\delta p\,\mathrm{d}\boldsymbol{x} = \int_\Gamma \delta p\,\mathrm{d}x^* \int_{-h}^{h} \frac{\partial v_{sx^*}}{\partial x^*}\mathrm{d}y^* + \int_\Gamma \delta p\,\mathrm{d}x^* \int_{-h}^{h} \frac{\partial v_{sy^*}}{\partial y^*}\mathrm{d}y^*$$
$$= \int_\Gamma \left(2h\left\langle\frac{\partial v_{sx^*}}{\partial x^*}\right\rangle + [v_{sy^*}]_{-h}^{h}\right)\delta p\,\mathrm{d}x^*;\ \int_{\Omega_c} n(\boldsymbol{v}_f - \boldsymbol{v}_s)\cdot\nabla\delta p\,\mathrm{d}\boldsymbol{x} = -\int_\Gamma 2h\,k_f\frac{\partial p}{\partial x^*}\frac{\partial\delta p}{\partial x^*}\,\mathrm{d}x^*, \tag{2.20}$$

where we have used the notations

$$\left\langle \frac{\partial v_{sx^*}}{\partial x^*} \right\rangle = \frac{v_{sx^*}|_{\Gamma^+} + v_{sx^*}|_{\Gamma^-}}{2}$$

and

$$[v_{sy^*}]_{-h}^{h} = v_{sy^*}|_{\Gamma^+} - v_{sy^*}|_{\Gamma^-} = [\![ v_{sy^*} ]\!].$$

Box 2 summarises the mixed variational form in the variables $\boldsymbol{u}$ and $p$ of the governing equations where we account for the fluid flow exchange through $\Gamma$.

$$\int_\Omega (2G\boldsymbol{e} + (K\epsilon - bp)\mathbf{1}) : \nabla(\delta\boldsymbol{u})\,\mathrm{d}\boldsymbol{x} - \int_{\partial_t\Omega} \bar{\boldsymbol{t}} \cdot \delta\boldsymbol{u}\,\mathrm{d}s - \int_\Gamma p\boldsymbol{n}_\Gamma \cdot [\![\delta\boldsymbol{u}]\!]\,\mathrm{d}s = 0\,;$$

$$\int_\Omega \frac{n}{K_f}\frac{\partial p}{\partial t}\delta p\,\mathrm{d}\boldsymbol{x} + \int_\Omega \nabla\cdot\boldsymbol{v}_s\,\delta p\,\mathrm{d}\boldsymbol{x} + \int_\Omega k_f \nabla p\cdot\nabla\delta p\,\mathrm{d}\boldsymbol{x} + \int_{\partial_v\Omega} \bar{v}\delta p\,\mathrm{d}s + \int_\Gamma \frac{2hn}{K_f}\frac{\partial p}{\partial t}\delta p\,\mathrm{d}x^*$$
$$+ \int_\Gamma \left(2h\left\langle \frac{\partial v_{sx^*}}{\partial x^*}\right\rangle + [\![ v_{sy^*} ]\!]\right)\delta p\,\mathrm{d}x^* - \int_\Gamma 2hk_f \frac{\partial p}{\partial x^*}\frac{\partial \delta p}{\partial x^*}\,\mathrm{d}x^* = 0$$

**Box 2.** Weak Form of the Governing Equations.

## 3. Numerical solution of the hydromechanical coupled problem

In this section we describe the fully discrete equations of the weak form reported in Box 2. These are obtained by applying the XFEM for the space discretisation and the backward Euler method for the time discretisation. The enrichment functions are represented by the Heaviside function to model functions with discontinuity jumps across $\Gamma$; the distance signed function to $\Gamma$ to model functions that are continuous but not differentiable with a discontinuity jump in the normal derivative; and singular functions to model the $\sqrt{r}$-singularity at the crack tip. For keeping the generality of the treatment, these interpolations are here considered for both the displacement field $\boldsymbol{u}$ and the pore pressure field $p$.

### 3.1. Space and time discretisation of the coupled problem

The domain $\Omega$ is discretised into finite elements. For each element the displacement and pore pressure are interpolated by the shape functions $N_{ar}^{\ell}$ and $N_{pr}^{\ell}$, respectively, with the index $\ell$ referring to the node within the element and the index $r$ referring to the type of interpolation function. Standard interpolation functions correspond to the index $r = 1$, whereas discontinuity and near tip singularity enrichment functions correspond to the indices $r = 2, 3$, respectively. The nodes are thus grouped in sets, with $I$ denoting the set of standard finite element nodes, $J$ the set of nodes used to capture the effects of the discontinuity through the Heaviside step function, and $K$ the set of nodes used for the near tip asymptotic functions. Consequently, we denote by $(\boldsymbol{a}_1^i, p_1^i)$ the standard displacement and pressure degree of freedom associated with the nodes $i \in I$, by $(\boldsymbol{a}_2^j, p_2^j)$ the enriched degrees of freedom associated with the nodes $j \in J$ and by $(\boldsymbol{a}_3^k, p_3^k)$ the additional degrees of freedom associated with the nodes $k \in K$. The XFEM approximation for the displacement and pressure fields is thus given by

$$\begin{aligned}
\boldsymbol{u}(\boldsymbol{x}) &= \sum_{i\in I} N_{a1}^i(\boldsymbol{x})\,\boldsymbol{a}_1^i + \sum_{j\in J} N_{a2}^j(\boldsymbol{x})\,\boldsymbol{a}_2^j + \sum_{k\in K}\sum_{\ell=1}^{4} N_{a3}^{k\ell}(\boldsymbol{x})\,\boldsymbol{a}_3^{k\ell} \\
p(\boldsymbol{x}) &= \sum_{i\in I} N_{p1}^i(\boldsymbol{x})\,p_1^i + \sum_{j\in J} N_{p2}^j(\boldsymbol{x})\,p_2^j + \sum_{k\in K} N_{p3}^k(\boldsymbol{x})\,p_3^k,
\end{aligned} \tag{3.1}$$

where the enriched shape functions $N_{a2}^j$, $N_{p2}^j$, $N_{a3}^{k\ell}$ and $N_{p3}^j$ are defined in terms of the standard shape functions $N_{a_1}^j$ and $N_{p1}^j$ as follows:

$$\begin{aligned}
N_{a2}^j(\boldsymbol{x}) &= N_{a1}^j(H(\boldsymbol{x}) - H(\boldsymbol{x}_j)), \\
N_{p2}^j(\boldsymbol{x}) &= N_{p1}^j(Z(\boldsymbol{x}) - Z(\boldsymbol{x}_j)), \\
N_{a3}^{k\ell}(\boldsymbol{x}) &= N_{a1}^k(F^\ell(\boldsymbol{x}) - F^\ell(\boldsymbol{x}_k)) \ \text{ for } \ \ell = 1,\ldots,4, \\
N_{p3}^k(\boldsymbol{x}) &= N_{p1}^k(G(\boldsymbol{x}) - G(\boldsymbol{x}_k)),
\end{aligned} \tag{3.2}$$

where $H$ denotes the Heaviside step shape function centred at the discontinuity and $Z$ is the signed distance functions of $\boldsymbol{x}$ to $\Gamma$, given by, respectively,

$$H = \begin{cases} 1 & \text{if } \boldsymbol{x} \in \Omega^+; \\ -1 & \text{if } \boldsymbol{x} \in \Omega^-. \end{cases} \qquad Z = \begin{cases} \mathrm{dist}(\boldsymbol{x};\Gamma) & \text{if } \boldsymbol{x} \in \Omega^+; \\ -\mathrm{dist}(\boldsymbol{x};\Gamma) & \text{if } \boldsymbol{x} \in \Omega^-, \end{cases} \tag{3.3}$$

with $\mathrm{dist}(\boldsymbol{x};\,\Gamma)=\inf\{|x-y|:\,y\in\Gamma\}$, whereas $F^{\ell}$, $\ell=1,\ldots,4$, and $G$ are the enriched tip basis, defined as

$$\{F^{\ell}(r,\theta)\}_{\ell=1}^{4}=\{\sqrt{r}\cos\theta/2,\sqrt{r}\sin\theta/2,\sqrt{r}\sin\theta/2\sin\theta,\sqrt{r}\cos\theta/2\sin\theta\}$$
$$G(r,\theta)=\sqrt{r}\sin\theta/2, \tag{3.4}$$

with $(r,\theta)$ the local polar coordinates of $\boldsymbol{x}\in\Omega\backslash\Gamma$ at the crack tip. The XFEM displacement, pressure and corresponding gradient are therefore represented as follows:

$$\boldsymbol{u}=\boldsymbol{N}_{a1}\boldsymbol{a}_1+\boldsymbol{N}_{a2}\boldsymbol{a}_2+\boldsymbol{N}_{a3}\boldsymbol{a}_3\quad p=\boldsymbol{N}_{p1}\boldsymbol{p}_1+\boldsymbol{N}_{p2}\boldsymbol{p}_2+\boldsymbol{N}_{p3}\boldsymbol{p}_3$$
$$\nabla\boldsymbol{u}=\boldsymbol{B}_{a1}\boldsymbol{a}_1+\boldsymbol{B}_{a2}\boldsymbol{a}_2+\boldsymbol{B}_{a3}\boldsymbol{a}_3\quad \nabla p=\boldsymbol{B}_{p1}\boldsymbol{p}_1+\boldsymbol{B}_{p2}\boldsymbol{p}_2+\boldsymbol{B}_{p3}\boldsymbol{p}_3, \tag{3.5}$$

where we have denoted by $\boldsymbol{a}_1=(a_1^i)_{i\in I}$, $\boldsymbol{a}_2=(a_2^j)_{j\in J}$, $\boldsymbol{a}_3=(a_3^k)_{k\in K}$ and $\boldsymbol{p}_1=(p_1^i)_{i\in I}$, $\boldsymbol{p}_2=(p_2^j)_{j\in J}$, $\boldsymbol{p}_3=(p_3^k)_{k\in K}$ the set of all standard and enriched displacement and pressure degrees of freedom, respectively, and $\boldsymbol{B}_{ar}=\nabla\boldsymbol{N}_{ar}$ and $\boldsymbol{B}_{pr}=\nabla\boldsymbol{N}_{pr}$, for $r=1,2,3$, denote the gradient of the standard and enriched shape functions of the displacement and pressure fields, respectively. Correspondingly, we have

$$\boldsymbol{v}_s=\boldsymbol{N}_{a1}\dot{\boldsymbol{a}}_1+\boldsymbol{N}_{a2}\dot{\boldsymbol{a}}_2+\boldsymbol{N}_{a3}\dot{\boldsymbol{a}}_3\ \nabla\cdot\boldsymbol{v}_s=\boldsymbol{m}^T(\boldsymbol{B}_{a1}\boldsymbol{a}_1+\boldsymbol{B}_{a2}\boldsymbol{a}_2+\boldsymbol{B}_{a3}\boldsymbol{a}_3)$$
$$\dot{p}=\boldsymbol{N}_{p1}\dot{\boldsymbol{p}}_1+\boldsymbol{N}_{p2}\dot{\boldsymbol{p}}_2+\boldsymbol{N}_{p3}\dot{\boldsymbol{p}}_3\ \nabla\dot{p}=\boldsymbol{B}_{p1}\dot{\boldsymbol{p}}_1+\boldsymbol{B}_{p2}\dot{\boldsymbol{p}}_2+\boldsymbol{B}_{p3}\dot{\boldsymbol{p}}_3, \tag{3.6}$$

which, replaced into the weak form of the governing equations (see Box 2), leads to the following coupled system of equations:

$$\int_{\Omega}\boldsymbol{B}_{ar}^T\boldsymbol{\sigma}\,\mathrm{d}\Omega+\int_{\Gamma}p\boldsymbol{N}_{ar}^T\boldsymbol{n}_{\Gamma}\,\mathrm{d}x^*-\int_{\partial_t\Omega}\boldsymbol{N}_{ar}^T\bar{\boldsymbol{t}}\,\mathrm{d}x^*=0$$
$$\int_{\Omega}\boldsymbol{N}_{pr}^T\nabla\cdot\boldsymbol{v}_s\,\mathrm{d}\Omega+\int_{\Omega}\boldsymbol{N}_{pr}^T\frac{\partial p}{\partial t}\frac{1}{K_f}\,\mathrm{d}V-\int_{\Omega}\boldsymbol{B}_{pr}^T\boldsymbol{w}\,\mathrm{d}\Omega+\int_{\Gamma}\boldsymbol{N}_{pr}^T[\![\boldsymbol{w}]\!]\cdot\boldsymbol{n}\,\mathrm{d}x^*+\int_{\partial\Omega}\boldsymbol{N}_{pr}^T\bar{v}\,\mathrm{d}x^*=0, \tag{3.7}$$

for $r=1,2,3$, which can be written in matrix form as

$$\boldsymbol{C}\dot{\boldsymbol{x}}+\boldsymbol{K}\boldsymbol{x}+\boldsymbol{f}=\boldsymbol{0}, \tag{3.8}$$

where $\boldsymbol{x}^T=[\boldsymbol{a}_1,\boldsymbol{a}_2,\boldsymbol{a}_3,p_1,p_2,p_3]$ is the vector of nodal unknowns whereas the matrices $\boldsymbol{C}$, $\boldsymbol{K}$ and $\boldsymbol{f}$ are given in Appendix A.

### 3.2. Time discretisation

The discrete equation (3.8) represents a system of ordinary differential equations which we discretise in time using the backward Euler scheme, that is,

$$\boldsymbol{F}_{n+1}=\boldsymbol{C}_{n+1}\frac{\Delta\boldsymbol{x}}{\Delta t}+\boldsymbol{K}_{n+1}\boldsymbol{x}_{n+1}+\boldsymbol{f}_{n+1}=\boldsymbol{0}, \tag{3.9}$$

where $\Delta\boldsymbol{x}=\boldsymbol{x}^{n+1}-\boldsymbol{x}^n$ and $\Delta t=t^{n+1}-t^n$, whereas $(\boldsymbol{x}^{n+1},\boldsymbol{x}^n)$ denote the unknowns at time $t^{n+1}$ and $t^n$, respectively. Since the matrices $\boldsymbol{C}_{n+1}$ and $\boldsymbol{K}_{n+1}$ are full, the resulting algebraic system of equations is fully coupled.

## 4. Semianalytical solution of the flow problem in porous cracked problem

In this section we review briefly the method of solution of the 2*d* steady-state flow in a fractured porous media using the complex potential method [4,5,7] specialised for different boundary conditions on $\Gamma$. The application of this method and the enforcement of the boundary conditions on $\Gamma$ transform the original Laplace equation into a singular integral equation of the first kind which is then solved numerically using a collocation method and numerical quadrature [6].

### 4.1. General analytical solution of the problem

We consider an isotropic saturated porous infinite domain $\Omega$ that contains a linear discontinuity $\Gamma$ modelled by a segment. We assume that $\Omega$ is subject to a steady-state flow $q_\infty$ which is inclined of an angle $\beta$ with respect to the direction of the rectilinear crack $\Gamma$, see Fig. 2. Under the assumption of steady-state flow, the poroelasticity equations in Box 1 uncouple in the Laplace equation for the pore pressure

$$\nabla\cdot\nabla p=\frac{\partial^2 p}{\partial x^2}+\frac{\partial^2 p}{\partial y^2}=0\quad\text{for}\quad(x,y)\in\Omega\setminus\Gamma \tag{4.1}$$

and in the equations of linear elasticity for the effective stress. The general solution of (4.1) can then be expressed in terms of the Goursat–Muskhelishvili potential function [4]. If we denote by $\hat{x}=x+iy$ the complex variable with $(x,y)\in\Omega$ and assume

$$p(\hat{x})=2\mathrm{Re}(\Phi(\hat{x})), \tag{4.2}$$

with $\Phi(\hat{x})$ of the following form:

$$\Phi(\hat{x})=\frac{q_\infty}{2}\hat{x}e^{-i\beta}+\bar{\Phi}(\hat{x}), \tag{4.3}$$

where $\bar{\Phi}=\bar{\Phi}(\hat{x})$ is an analytic function in $\Omega\backslash\Gamma$ and singular on $\Gamma$, it is not difficult to show that (4.2) is solution of (4.3) in $\Omega\backslash\Gamma$. The specific choice of $\bar{\Phi}(\hat{x})$ depends on the boundary conditions to meet on $\Gamma$. We consider here the case where a prescribed pressure is given along $\Gamma$, see Fig. 3a, and a prescribed Poiseuille flow is given along $\Gamma$, see Fig. 3b.

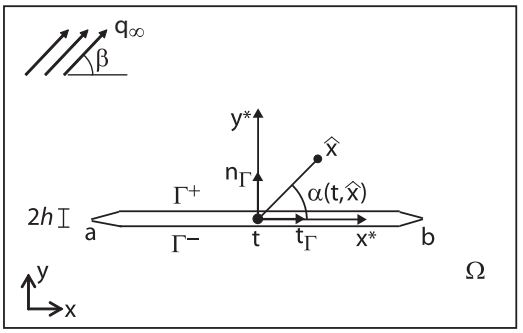


**Fig. 2.** Single crack in an infinite plate. Definition of the notation. Distance of each point $t \in \Gamma$ on the crack to a point $\hat{x} = x + iy \in \Omega$.

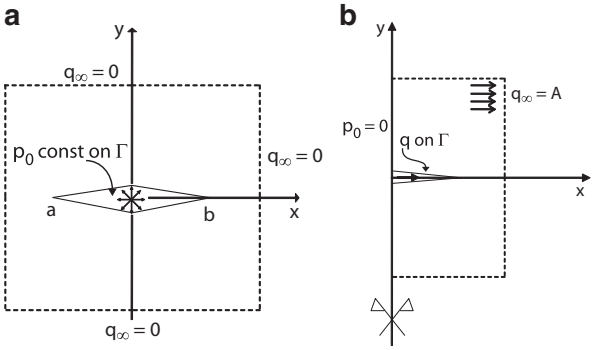


**Fig. 3.** Single crack in an infinite plate: (*a*) subjected to constant pressure $p_0$, and (*b*) subjected to constant flow $q_\infty$ at the infinity.

*4.1.1. Prescribed pressure inside the crack*

For this case, we can consider the following representation of the potential function [4,5]

$$\bar{\Phi}(\hat{x}) = \frac{1}{2\pi}\int_\Gamma \frac{\phi(t)}{t-\hat{x}}dt \tag{4.4}$$

with $\phi(t)$ an unknown density function integrable and continuous on $\Gamma$ which must be found by enforcing the condition that $p(\hat{x}(t)) = p_0(t)$ for $t \in \Gamma$, where $p_0(t)$ is a prescribed variation of the pressure along $\Gamma$. The potential $\bar{\Phi}$ is an integral of Cauchy along $\Gamma$, it is analytic in $\Omega\backslash\Gamma$ and approaches zero for large values of $|t-\hat{x}|$. By combining (4.4), (4.3) and (4.2) we have

$$p(\hat{x}) = q_\infty \mathrm{Re}(\hat{x}e^{-i\beta}) + \frac{1}{\pi}\int_\Gamma \frac{\phi(t)}{|t-\hat{x}|}dt \quad \hat{x} \in \Omega \setminus \Gamma, \quad t \in \Gamma, \tag{4.5}$$

so that the right specification of $\phi(t)$ is obtained by solving the following singular integral equation:

$$q_\infty \mathrm{Re}(t_0 e^{-i\beta}) + \frac{1}{\pi}\int_\Gamma \frac{\phi(t)}{|t-t_0|}dt = p_0(t_0) \quad t_0 \in \Gamma. \tag{4.6}$$

*4.1.2. Prescribed Poiseuille flow inside the crack*

For this case we have the following representation of the potential function [4,5]

$$\bar{\Phi}(\hat{x}) = \int_\Gamma \phi(t)\ln(\hat{x}-t)dt, \tag{4.7}$$

with $\phi(t)$ the unknowns density function integrable and continuous on $\Gamma$ to be found by enforcing the Neumann boundary condition on $\Gamma$ expressing the condition of a Poiseuille flow inside the crack, i.e. condition (2.14). In order to enforce (2.14), it is more convenient to express the complex potential $\Phi$ of (4.3) in terms of the flow $q$ inside the cavity. To do so, we express first $\phi(t)$ as follows (see Appendix B for the details of the derivation)

$$\phi(t) = \frac{1}{2\pi k_f}\frac{\partial q}{\partial x^*}. \tag{4.8}$$

Now, by combining (4.8) with (4.7) and replaced first in (4.3) and then in (4.2), we have the following representation of the fluid pressure:

$$p(\hat{x}) = q_\infty \mathrm{Re}(\hat{x}e^{-i\beta}) + \frac{1}{\pi k_f}\int_\Gamma \frac{\partial q}{\partial x^*}\ln|\hat{x}-t|dt \quad \text{for } \hat{x} \in \Omega \setminus \Gamma, \quad t \in \Gamma. \tag{4.9}$$

Now (2.14) can also be written as

$$\frac{\partial p}{\partial x^*} = -\frac{q(t)}{k_d} \quad \text{for } t \in \Gamma, \tag{4.10}$$

so that by integrating over $\Gamma$, we have

$$p(t_0) - p(0) = -\int_0^{t_0} \frac{q(t)}{k_d}\, dt \quad \text{for } t_0 \in \Gamma. \tag{4.11}$$

By replacing thus (4.9) into (4.11) we are led to the problem of finding $q(t)$ for $t \in \Gamma$ which solves the following singular integral equation:

$$q_\infty \mathrm{Re}(t_0 e^{-i\beta}) + \frac{1}{\pi k_f}\int_\Gamma \frac{\partial q(t)}{\partial x^*} \ln|t_0 - t| dt = -\int_0^{t_0} \frac{q(t)}{k_d}\, dt \quad t_0 \in \Gamma, \tag{4.12}$$

where we have assumed that $p(0) = 0$.

### 4.2. Numerical solution of the integral singular equations

For the numerical solution of the singular integral equations (4.6) and (4.12), we use the methods proposed in [6] where, however, an appropriate quadrature formula must be chosen depending on the type of singularity at the end points $a$ and $b$. At the points of geometrical singularity $a$ and $b$, the function $\phi$ can indeed be either bounded or have an integrable singularity, and this depends on the physical arguments of the problem. When the unknown function is the pore pressure potential, as is usually the case, $\phi$ is bounded at the points $a$ and $b$. For this case, then [6] suggest the Gauss–Chebyshev quadrature formula where the points of integration $t_j \in \Gamma$, $j = 1, \ldots, N$, are the zeros of the Chebyshev polynomial of the first kind of degree $N$ whereas the collocation points $t_{0i} \in \Gamma$, $i = 1, \ldots, N+1$, where the pore pressure $p$ must be evaluated, are the zeros of the Chebyshev polynomial of second kind of degree $N+1$.

Denoting by $w(x*)$ the fundamental solution of the singular integral equation [4], and $g(x^*)$ a bounded function, continuous in $[a, b]$, we can write $\phi(x^*)$ as follows

$$\phi(x^*) = w(x^*)g(x^*), \quad a < x^* < b. \tag{4.13}$$

A numerical method for the determination of $g(x^*)$ will be developed in the following subsection for both Dirichlet and Neumann boundary conditions. The values of the function $\phi$ are then determined at some specific nodes, as solution of a system of linear equations.

#### 4.2.1. Prescribed pressure inside single crack

In this case $q_\infty = 0$ and the pressure distribution inside the crack $p_0(t_0)$ is known for every $t_0 \in \Gamma$. Thus (4.6) becomes

$$p_0(t_0) = \frac{1}{\pi}\int_\Gamma \frac{\phi(t)}{|t - t_0|} dt. \tag{4.14}$$

To evaluate the pore pressure $p$ at $\hat{x} \in \Omega$, we need to compute first the unknown density $\phi$ on $\Gamma$ so that (4.14) is satisfied along the crack. Following [5,6] we solve the singular integral equation (4.14) using the collocation method and Gauss quadraturae. That is, we enforce (4.14) at a discrete set of collocation points $t_{0i} \in \Gamma$, with $i = 1, \ldots, N+1$, and then solve by Gauss-Chebyshev quadratures, using the set of integration points $t_j \in \Gamma$, with $j = 1, \ldots, N$, the integral appearing in (4.14) evaluated at the collocation points. In this manner, we obtain a of $N+1$ linear equations, one equation for each collocation point, is obtained which reads as follows:

$$p_0(t_{0i}) = \frac{1}{\pi}\sum_{j=1}^{N} \frac{w_j g_j}{|t_j - t_{0i}|}, \quad i = 1, \ldots, N+1, \tag{4.15}$$

where

$$w_j = w(t_j) = \frac{\pi}{N+1}\sin^2\left(\frac{j\pi}{N+1}\right).$$

Each equation in (4.15) depends on the $N$ unknowns $g_j = g(t_j)$ given by the value of $g$ at the integration point $j$, for $j = 1, \ldots, N$. As a result, (4.15) appears as a system overdetermined of $N+1$ equations in $N$ unknowns, which we solve following [5,6] that suggest to choose $N$ to be an even integer and drop the equation $N/2 + 1$.

The fundamental function $w_j$ has been selected in such a way that the corresponding weight function and $t_j$ correspond to the zeros of the orthogonal polynomials related to the particular Gaussian quadrature. For the case of integrable singularities at the end points, the orthogonal polynomials reduce to the Chebyshev polynomials of first kind, thus the collocation and the integration points in the range $[a, b]$ that represents the crack $\Gamma$, will be given by

$$\begin{aligned} t_j &= \frac{b-a}{2}\zeta_j + \frac{b+a}{2} \quad j = 1, \ldots, N \\ t_{0i} &= \frac{b-a}{2}\eta_i + \frac{b+a}{2} \quad i = 1, \ldots, N+1, \end{aligned} \tag{4.16}$$

where $\zeta_j$ are the roots of the Chebyshev polynomials of second kind of order $N$, whereas $\eta_i$ are the roots of the Chebyshev polynomials of the first kind of order $(N+1)$ in the interval $[-1, 1]$. The points $\zeta_j$ and $\eta_i$ are thus given as follows [6]:

$$\zeta_j = \cos\left(\frac{j\pi}{N+1}\right), \quad j = 1, \ldots, N$$
$$\eta_i = \cos\left(\frac{\pi(2i-1)}{2(N+1)}\right), \quad i = 1, \ldots, N+1. \tag{4.17}$$

Once $g_j$, $j = 1, \ldots, N$, are computed, the pressure and the gradient of the pressure in the entire domain $\Omega$ can be evaluated at any point $\hat{x} \in \Omega \setminus \Gamma$ as follows:

$$p(\hat{x}) = \frac{1}{\pi}\sum_{j=1}^{n}\frac{w_j g_j}{|t_j - \hat{x}|}$$
$$\nabla_{\hat{x}} p(\hat{x}) = \frac{1}{2}\left(\frac{\partial p(\hat{x})}{\partial x} - i\frac{\partial p(\hat{x})}{\partial y}\right) \tag{4.18}$$
$$= \frac{1}{2\pi}\sum_{j=1}^{n} w_j g_j \frac{\cos\alpha(t_j, \hat{x})}{|t_j - \hat{x}|^2} - i\frac{1}{2\pi}\sum_{j=1}^{n} w_j g_j \frac{\sin\alpha(t_j, \hat{x}_i)}{|t_j - \hat{x}_i|^2},$$

where $\alpha$ is the angle formed by the vector $t_j\hat{x}$ and the axis $O\hat{x}$. The full algorithm of the numerical integration scheme of the semianalytical solution is summarised in Box 3.

*4.2.2. Prescribed Poiseuille flow inside the crack*

Let us now consider the case of the single straight crack $\Gamma$, as shown in Fig. 2, in an infinite fully saturated porous medium subjected to a uniform pressure gradient $(A, 0)$, parallel to the crack $\Gamma$. The pressure field at infinity is then of the form $p_\infty(\hat{x}) = 2\mathrm{Re}(q_\infty \hat{x} e^{-i\beta}/2) = Ax$ where $x = \mathrm{Re}(\hat{x})$ is the real part of $\hat{x}$. Consider now $\Gamma$ parameterised by the curvilinear coordinate $x^* \in [-1, 1]$. By integrating by parts the integral over $\Gamma$ which appears in (4.9), we obtain

$$p(\hat{x}) = Ax + \frac{k_d}{2\pi k_f}\int_{-1}^{1}\frac{\partial p}{\partial x^*}\frac{\hat{x} - x^*}{|\hat{x} - x^*|^2}\cdot t_\Gamma(x^*)dx^*, \tag{4.19}$$

where $t_\Gamma(x^*)$ is the unit tangent vector at $\Gamma$ at $x^* \in \Gamma$, and we have taken into account of (4.10) and used the condition that $q(1) = q(-1)$. Let us assume the global Cartesian coordinate system with origin at the middle of the crack $\Gamma$ and the $x-$ axis along the crack. By the symmetry of the geometry and boundary conditions, we can infer that $p(-x, y) = -p(x, y)$, $\partial p(-x, y)/\partial x^* = -\partial p(x, y)/\partial x^*$ and $p(0, 0) = 0$. As a result, at $x_0 \in \Gamma = [-1, 1]$, the pressure can be expressed as follows:

$$p(x_0, 0) = \int_0^{x_0}\frac{\partial p}{\partial x^*}dx^*. \tag{4.20}$$

By combining (4.19) and (4.20), and taking into account of the symmetry of the pore pressure distribution along the crack, we are led to the problem of finding the function $\partial p/\partial x^*$ defined on $[0, 1]$ such that for any $x_0 \in [0, 1]$ there holds

$$\int_0^{x_0}\frac{\partial p}{\partial x^*}dx^* - \frac{k_d}{\pi k_f}\int_0^1\left(\frac{\partial p(x^*)}{\partial x^*} - \frac{\partial p(x_0)}{\partial x^*}\right)\frac{x_0}{x^{*2} - x_0^2}dx^* - \frac{k_d}{2\pi k_f}\frac{\partial p(x_0)}{\partial x^*}\ln\frac{1 - x_0}{1 + x_0} = Ax_0. \tag{4.21}$$

In order to solve (4.21), also here we apply the method of the fundamental solutions [4], and look for a solution in the form $\partial p/\partial x^* = w(x^*)g(x^*)$, with $g(x^*)$ a bounded continuous function in $[-1, 1]$ and $w(x*)$ the fundamental solution of the singular integral equation [4]. By replacing therefore $\partial p/\partial x^* = w(x^*)g(x^*)$ into (4.21), we are led to the problem of finding for any $x_0 \in [0, 1]$ the value of $g(x_0)$ such that there holds

$$\int_0^{x_0} w(x^*)g(x^*)dx^* - \frac{k_d x_0}{\pi k_f}\int_0^1\frac{w(x^*)g(x^*) - w(x_0)g(x_0)}{x^{*2} - x_0^2}dx^* - \frac{k_d}{2\pi k_f}w(x_0)g(x_0)\ln\frac{1 - x_0}{1 + x_0} = Ax_0, \tag{4.22}$$

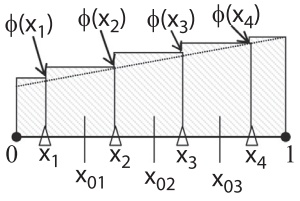


**Fig. 4.** Integration points $x_i$, $i = 1, \ldots, N+1$ and collocation points $x_{0j}$, $j = 1, \ldots, N$ along the crack for $N = 3$.

**Given:** $a,\ b,\ N,\quad \text{and}\quad p_0 \text{ on } \Gamma;$

**Compute:** for $i = 1, ..., N+1$

$$\eta_i = \cos\left(\frac{\pi(2i-1)}{2(N+1)}\right)$$
$$t_{0i} = \frac{b-a}{2}\eta_i + \frac{b+a}{2}$$

next $i$

for $j = 1, ..., N$

$$\zeta_j = \cos\left(\frac{j\pi}{N+1}\right)$$
$$t_j = \frac{b-a}{2}\zeta_j + \frac{b+a}{2}$$
$$w_j = \frac{\pi}{n+1}\sin^2\left(\frac{j\pi}{N+1}\right)$$

next $j$

for $i = 1, ..., N+1$

for $j = 1, ..., N$

$$B_{ij} = \frac{w_j}{|t_j - t_{0i}|}$$

next $j$

next $i$

**Solve:**
$$\sum_{j=1}^{N} B_{ij} g_j = \pi p_0(t_{0i}), \quad i = 1, ..., N+1$$

**Find:** for $\hat{x} \in \Omega \setminus \Gamma$,

$$p(\hat{x}) = \frac{1}{\pi}\frac{w_j g_j}{|t_j - \hat{x}|}$$
$$\nabla_{\hat{x}} p(\hat{x}) = \frac{1}{2\pi}\sum_{j=1}^{N} w_j g_j \frac{\cos\alpha(t_j,\hat{x})}{|t_j-\hat{x}|^2} - i\frac{1}{2\pi}\sum_{j=1}^{N} w_j g_j \frac{\sin\alpha(t_j,\hat{x})}{|t_j-\hat{x}|^2}$$

**End**

**Box 3.** Numerical integration algorithm for the semianalytical solution with prescribed pressure on $\Gamma$.

where the singularities at the end points have been removed. We solve numerically the singular integral equation (4.22) by enforcing (4.22) to hold at the collocation points $x_{0i} \in \Gamma$, $i = 1, \ldots, N+1$, and then by solving the integral in (4.22) by Gauss-Chebyshev quadraturae. If we therefore denote by $x_j$, $j = 1, \ldots, N$ the integration points on $\Gamma$ (see Fig. 4), we have then to solve the following system of linear equations in $g_j = g(x_j)$, $j = 1, \ldots, N$,

$$\sum_{j=1}^{i} w_j g_j - \frac{x_{0i} k_d}{\pi k_f}\left(\sum_{j=1}^{N}\frac{w_j g_j - w_i g_{0i}}{x_j^2 - x_{0i}^2}\right) - \frac{k_d}{2\pi k_f} w_i g_{0i} \ln\frac{1-x_{0i}}{1+x_{0i}} = A\, x_{0i} \quad \text{for } i = 1, \ldots, N+1, \tag{4.23}$$

where $w_i = x_{0i} - x_{0(i-1)}$ [5]. If we set

$$B_{ij} = w_j - \frac{k_d}{\pi k_f} T_{ij} \quad \text{if } j < i$$

**Table 1**
Poroelastic properties of the model problem of Examples 5.1 and 5.4.

| | |
|---|---|
| Young modulus, $E$ [GPa] | 30 |
| Poisson coefficient, $\nu$ | 0.2 |
| Water compressibility modulus, $K_f$ [GPa] | $1 \cdot 10^{18}$ |
| Biot's coefficient $b$ | 1 |
| Bulk permeability coefficient, $k_f$ [cm/s] | 1 |

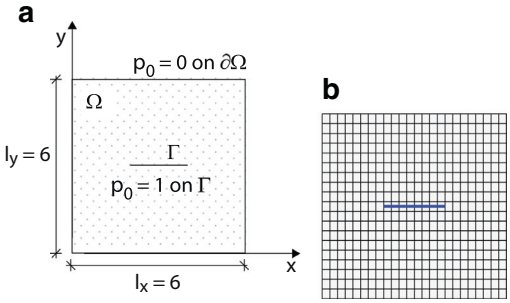


**Fig. 5.** (*a*) Geometry and boundary conditions of the model problem of Example 5.1. (*b*) Finite element mesh.

$$B_{ii} = \frac{1}{2}w_j - \frac{k_d}{\pi k_f}\sum_{k=1}^{N} T_{ik} - \frac{k_d}{2\pi k_f} g_{0i} \ln\frac{1-x_{0i}}{1+x_{0i}} \quad \text{if } i = j$$

$$B_{ij} = -\frac{k_d}{\pi k_f} T_{ij} \quad \text{if } j > i,$$

with $T_{ij} = \frac{w_j x_{0i}}{x_j^2 - x_{0i}^2}$ when $i \neq j$, and $T_{ii} = 0$ when $i = j$, then it is not difficult to show, after some rearrangements, that (4.23) can be rewritten as follows:

$$\sum_{j=1}^{N} B_{ij} g_j - A x_{0i} = 0 \quad \text{for } i = 1, \ldots, N+1. \tag{4.24}$$

The solution of (4.24) allows the evaluation of the pressure at any point $\hat{x} \in \Omega$ using (4.22), whose discrete expression is given as follows

$$p(\hat{x}) = A\,\mathrm{Re}(\hat{x}) + \frac{k_d}{2\pi k_f}\sum_{j=1}^{N} w_j g_j \left( \frac{x_j - \hat{x}}{|x_j - \hat{x}|^2} - \frac{x_j + \hat{x}}{|x_j + \hat{x}|^2} \right) \cdot t_\Gamma(x_j), \tag{4.25}$$

where $x_j \in \Gamma$ for $j = 1, \ldots, N$ are the integration points of the Gauss-Chebyshev quadrature scheme. The complete algorithm is reported in Box 4.

## 5. Numerical examples

This section contains four examples that illustrate the performance of the XFEM for modelling the hydromechanical behaviour of a porous media $\Omega$ with an interior interface $\Gamma$. In the first two examples, we consider steady state flow and compare the XFEM results against the semianalytical ones, assuming Dirichlet and Neumann boundary conditions on the interface $\Gamma$, respectively. In the third example, we validate our XFEM flow model against experimental observations on the permeability coefficient for different sample widths. In the last example, finally, we analyse a fully hydromechanical coupled problem to assess the influence of the flow pressure on the crack width for different ratios of the porous medium permeability to the crack permeability.

### 5.1. Prescribed pressure inside the crack

This example and the next one contain model problems where we assume steady-state flow and we solve by the XFEM and the semianalytical method. The objective is to verify the quality of the XFEM solution. Geometry and boundary conditions of the model problem of the first example are shown in Fig. 5 along with the finite element mesh used for the numerical results. The domain $\Omega$ is a square shaped body of fully saturated porous material with a straight crack $\Gamma$ at its interior. The crack $\Gamma$ is placed at the centre of the specimen and parallel to one of its sides. We assume drained conditions with zero pressure along the whole boundary $\partial\Omega$, and drained conditions also along $\Gamma$ with pressure $\bar{p} = 1$. No mechanical load is applied and displacement boundary conditions are introduced to remove rigid body motions. The mechanical properties of the block are given in Table 1.

The finite element mesh used for the simulation contains 480 quadrilateral elements with 20 elements along the $x-$ direction and 24 elements along the $y-$ direction so to have the crack $\Gamma$ intersecting the middle of each element. Quadratic shape functions have been used for the interpolation of the displacement field and bilinear shape functions for the interpolation of the pressure

**Given:** $a$, $b$, $N$ and $q_\infty = A$

**Compute:** for $i = 1, ..., N+1$

$$\eta_i = \cos\left(\frac{\pi(2i-1)}{2(N+1)}\right)$$
$$x_{0i} = \frac{b-a}{2}\eta_i + \frac{b+a}{2}$$
$$w_i = x_{0i} - x_{0(i-1)}$$

next $i$

for $j = 1, ..., N$

$$\zeta_j = \cos\left(\frac{j\pi}{N+1}\right)$$
$$x_j = \frac{b-a}{2}\zeta_j + \frac{b+a}{2}$$

next $j$

for $i = 1, ..., N+1$

for $j = 1, ..., N$

If $i \neq j$, $\quad T_{ij} = \dfrac{w_j x_{0i}}{x_j^2 - x_{0i}^2}$

else $T_{ii} = 0$.

If $j < i$ $\quad B_{ij} = w_j - \dfrac{k_d}{\pi k_f} T_{ij}$

else if $i = j$, $\quad B_{ii} = \dfrac{1}{2} w_i - \dfrac{k_d}{\pi k_f} \sum_{k=1}^{N} T_{ik} - \dfrac{k_d}{2\pi k_f} g_{0i} \ln \dfrac{1 - x_{0i}}{1 + x_{0i}}$

else $B_{ij} = -\dfrac{k_d}{\pi k_f} T_{ij}$.

next $j$

next $i$

**Solve:** $\displaystyle\sum_{j=1}^{N} B_{ij} g_j - A x_{0i}, \quad i = 1, ..., N+1$

**Find:** for $\hat{x} \in \Omega \setminus \Gamma$, $\quad x_j \in \Gamma$ for $j = 1, \ldots, N$

$$B_j(\hat{x}) = \left(\frac{x_j - \hat{x}}{|x_j - \hat{x}|^2} - \frac{x_j + \hat{x}}{|x_j + \hat{x}|^2}\right) \cdot t_\Gamma(x_j) \quad \text{for } j = 1, \ldots, N$$
$$p(\hat{x}) = A\,\mathrm{Re}(\hat{x}) + \frac{k_d}{2\pi k_f} \sum_{j=1}^{N} w_j g_j B_j(\hat{x}).$$

**End**

**Box 4.** Numerical integration algorithm for the semianalytical solution of Poiseuille flow inside the crack.

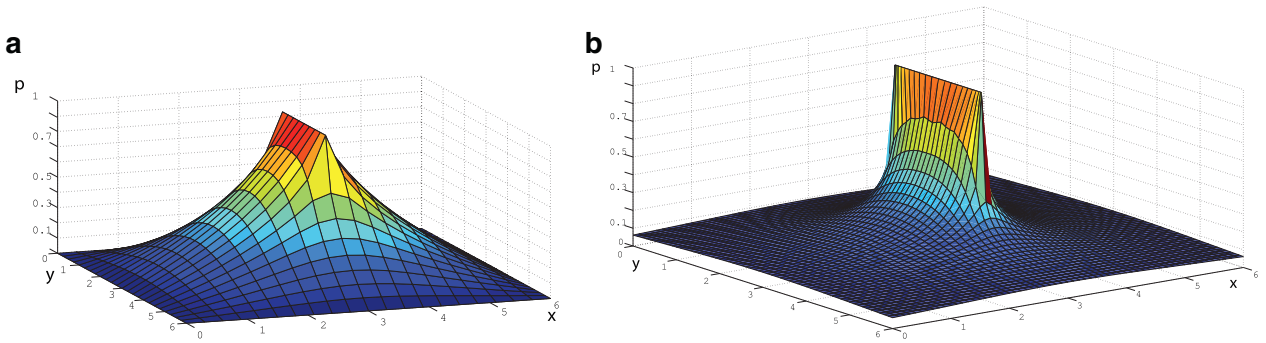


**Fig. 6.** Pressure field distribution computed with (*a*) the XFEM and (*b*) the semianalytical method.

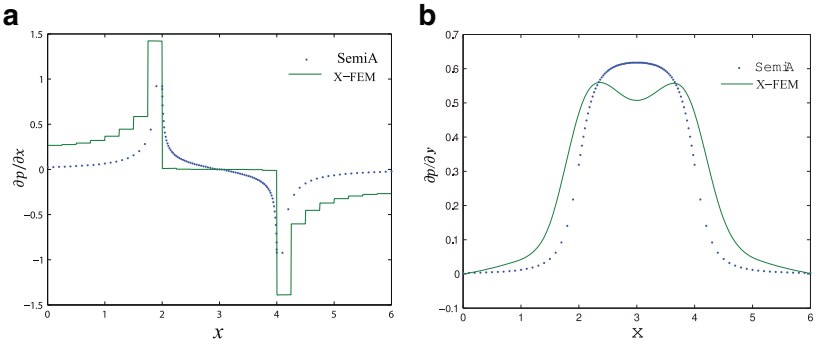


**Fig. 7.** Comparison of the semianalytical and XFEM solution. Variation of (*a*) $\partial p/\partial x$ along $y = 2.7$ and of (*b*)$\partial p/\partial y$ along $y = 3$.

field. For the integration of the discontinuous and singular shape functions, the number of Gauss integration points used in the enriched elements was 36 in the enriched elements which were not intersected by the crack $\Gamma$ and was 100 in the enriched elements which were intersected by the crack.

The semianalytical solution has been obtained by applying the algorithm described in Box 3 using $N = 92$ integration points and the boundary condition at the infinity $p_\infty = 0$ and $\tilde{p} = 1$ on $\Gamma$. The order $N$ of the Chebyshev polynomial has been chosen after comparing the semianalytical solution computed for different values of $N$. The pressure distribution in $\Omega$ obtained with the XFEM and the semianalytical method are displayed in Fig. 6 where, compared to the XFEM solution, the semianalytical solution presents a higher gradient near the interface. The enrichment of the pressure field by the distance function does not seem to improve the numerical approximation close to the crack given that the XFEM pressure gradient results tailored according to the distance gradient. To gain further insight on the flow near the crack, Fig. 7(*a*) and (*b*) display the variation of $\partial p/\partial x$ along $y = 2.7$ and of $\partial p/\partial y$ along $y = 3$, respectively. In both the variations, the XFEM solution presents higher gradient values away from the discontinuity. As for the variation of $\partial p/\partial x$ along $y = 2.7$ which is not exactly on the crack, we observe a change of sign at $x = 3$ for the semianalytical solution and zero tangential flow for both the solutions, though the XFEM solution presents zero tangential flow along the whole crack. In the porous matrix and very close to the crack tips, both the XFEM and the semianalytical solution are able to capture the crack tip singularity with a change of sign indicating that the fluid flows in opposite directions. As for the variation of $\partial p/\partial y$ along $y = 3$, which is used to compute the fluid that flows into the cavity, the XFEM solution presents a hat shape at the crack tips which is not displayed by the semianalytical solution. The semianalytical solution presents furthermore its maximum flow at the center of the crack and approaches to zero at the crack tips at variance of the behaviour displayed by the XFEM solution.

To analyse the quality of the XFEM approximation, several computations have been performed on meshes designed according to the remeshing strategy shown in Fig. 8. Fig. 9 shows the variation of the relative errors $\|p - p_{ref}\|_{L^2(\Omega)}/\|p_{ref}\|_{L^2(\Omega)}$, $\|\partial p/\partial x - \partial p_{ref}/\partial x\|_{L^2(\Omega)}/\|\partial p_{ref}/\partial x\|_{L^2(\Omega)}$ and $\|\partial p/\partial y - \partial p_{ref}/\partial y\|_{L^2(\Omega)}/\|\partial p_{ref}/\partial y\|_{L^2(\Omega)}$ with respect to the number of finite elements. The symbol $\|p\|_{L^2(\Omega)}$ denotes the $L^2$ norm of the field $p$, i.e. $\|p\|_{L^2(\Omega)} = \sqrt{\int_\Omega |p|^2\, dx}$, whereas the reference value $p_{ref}$ is an approximation of the exact solution taken as the XFEM solution of a very fine mesh of about 8000 elements (corresponding to the finite element mesh of 79 × 96 elements). The inspection of the convergence plots shows that XFEM solutions with an accuracy of at least 5% can be obtained with already few finite elements. The computation times obtained using an Intel Core i7 are given in Table 2 where one can appreciate that the computation is quite fast, given that in the case of steady-state flow, one is faced with the solution of a Laplacian equation where the major cost of the computation is given by the construction of the stiffness matrix of the enriched elements.

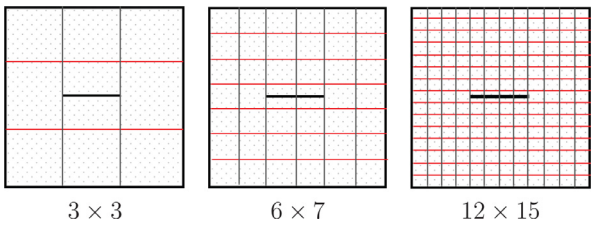


**Fig. 8.** Remeshing strategy.

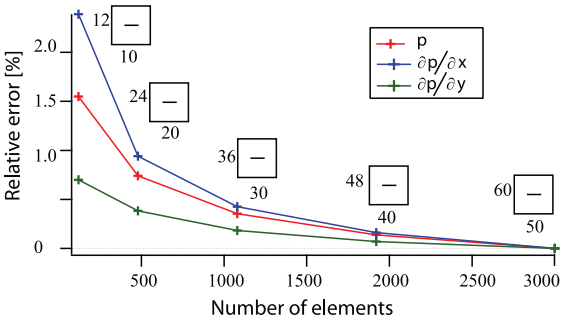


**Fig. 9.** Plots of the relative error of the pressure and of the fluid flow for different finite element meshes.

**Table 2**
CPU time with an Intel Core i7-4510U@2.00 GHz.

| $N_x \times N_y$ | Number of elements | Computation time [s] |
|---|---|---|
| $12 \times 10$ | 120 | 10 |
| $24 \times 20$ | 480 | 26 |
| $36 \times 30$ | 1080 | 34 |
| $48 \times 40$ | 1920 | 52 |
| $60 \times 50$ | 3000 | 60 |

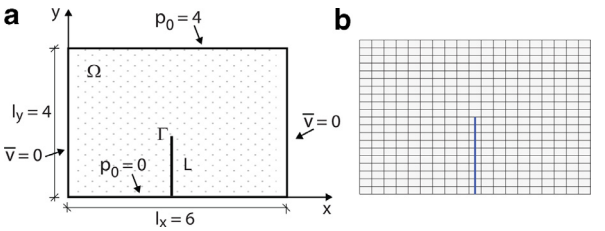


**Fig. 10.** (*a*) Geometry and boundary conditions of the model problem with Poiseuille flow inside the crack of Example 5.2. (*b*) Finite element mesh.

### *5.2. Poiseuille flow inside the crack*

As second model problem to verify the XFEM solution, we consider the case of a prescribed Poiseuille flow inside the crack $\Gamma$. In this case, the boundary condition on the interface $\Gamma$ is given by (2.14). The geometry and boundary conditions are displayed in Fig. 10 along with the finite element mesh used for the computations. The domain $\Omega$ is a rectangular shape body fully saturated with the straight crack $\Gamma$ parallel to the axis $y$ and starting on the boundary $\partial\Omega$ of $\Omega$. We assume drained boundary conditions with zero pressure on the edge $y = 0$ and pressure $p = 4$ on the edge $y = 4$. On the lateral faces, i.e. the edges $x = 0$ and $x = 6$, we assume impermeable boundary conditions, i.e. the fluid is not allowed flowing normal to the boundary, i.e. the normal component $\bar{v}$ of the velocity is zero on such edges. Also in this case, no mechanical load is applied and displacement boundary conditions are introduced to remove the rigid body motions. The mechanical properties of the block are the same as the ones of the previous example and are given in Table 1 as well.

The XFEM solution has been obtained using the finite element mesh displayed in Fig. 10, with quadratic shape functions for the interpolation of the displacement field and bilinear shape functions for that of the pressure field. We have then used 36 Gauss integration points in all the enriched finite elements. As for the semianalytical solution, this has been obtained by applying the algorithm described in the Box 4, using $N = 60$ integration points as order of the polynomial of Chebyshev, and taking $p_0(0, y) = 0$ and $p_\infty = x$ as boundary conditions.

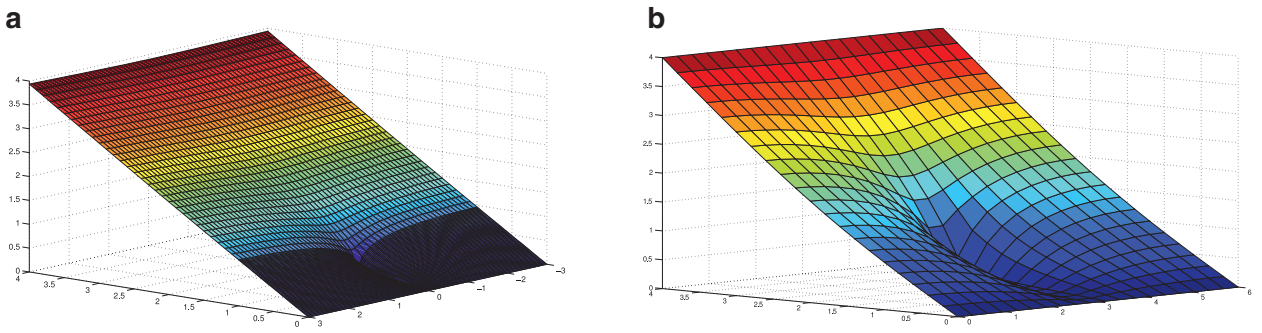


**Fig. 11.** Pressure field distribution for $\lambda = 1$. (*a*) Semianalytical solution and (*b*) XFEM solution.

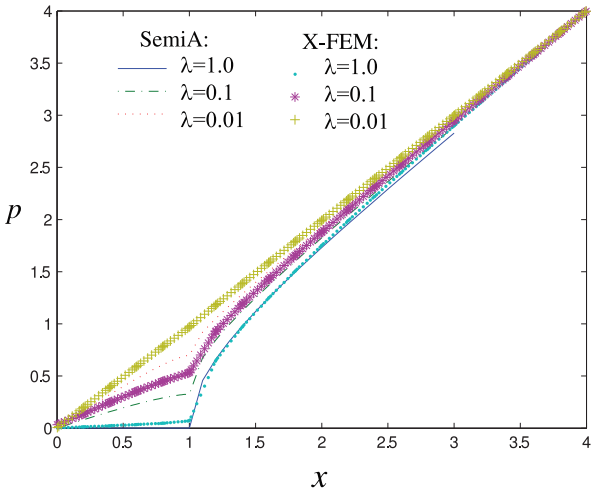


**Fig. 12.** Comparison of the semianalytical and XFEM solution. Variation of the pressure along the crack for different values of $\lambda = k_d/(2\pi k_f L)$.

For the analysis of the results, it is convenient to introduce the following dimensional parameter

$$\lambda = k_d/(2\pi k_f L),$$

with $L$ the crack length, which measures the ratio of permeabilities of the porous media surrounding the crack and the one of the crack. A higher value of $\lambda$ means that the fracture has a permeability higher than that of the surrounding porous medium and the fluid has therefore a tendency to flow in the fracture and then along the crack. As opposite, a low value of $\lambda$ means that the crack has a lower permeability, and the fluid will tend to avoid the crack which behaves as a barrier. The simulations have thus been carried out considering three different values of $\lambda$, a high one $\lambda = 1$, an intermediate one $\lambda = 0.1$ and a low one $\lambda = 0.01$.

The pressure distributions in $\Omega$ obtained with XFEM and the semianalytical method, assuming $\lambda = 1$, are displayed in Fig. 11, where also in this example we observe that the semianalytical solution presents a higher gradient near the interface than the XFEM solution. The pressure distribution in the crack as obtained by both methods are displayed in Fig. 12 for the said different values of $\lambda$. We observe that in the case of $\lambda = 1$, thus for high permeability of the cavity, both the semianalytical solution and the XFEM solution give a constant value of the pressure in the cavity, which in the example is equal to zero, consistently with the value prescribed by the boundary condition. For low permeability of the crack, corresponding to low values of $\lambda$, the pressure appears to be not affected by the presence of the crack. Figs. 13 and 14 display the variation of the pressure gradient components $\partial p/\partial x$ and $\partial p/\partial y$ along lines parallel to the crack, respectively, so that we can get an insight on how the flow is influenced by the presence of the crack under the boundary conditions that we are here examining. Since $\partial p/\partial y$ is related to the crack's tangential flow, a high permeable crack implies that the tangential flow is almost zero in the discontinuity, and the fluid thus flows almost entirely in the normal direction to the crack, whereas for a low permeable crack, the flow is unidirectional along $y$ direction, and the flow normal to the crack is zero. Such behaviours are captured by both the XFEM solution and the semianalytical solution. From the diagram shown in Fig. 14 we observe, however, that the normal flow computed with the semianalytical method has a maximum at $L/2$ as opposite to the XFEM solution which has its maximum at the crack tip.

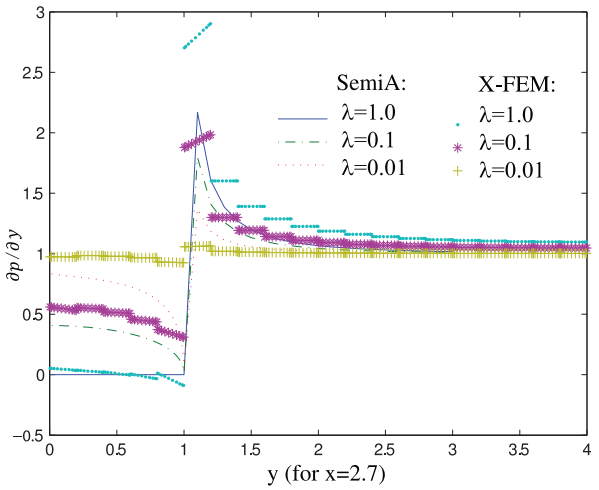


**Fig. 13.** Comparison of the semianalytical and XFEM solution. Variation of the pressure gradient component normal to the crack, $\partial p/\partial y$, along $x = 2.7$ for different values of $\lambda$.

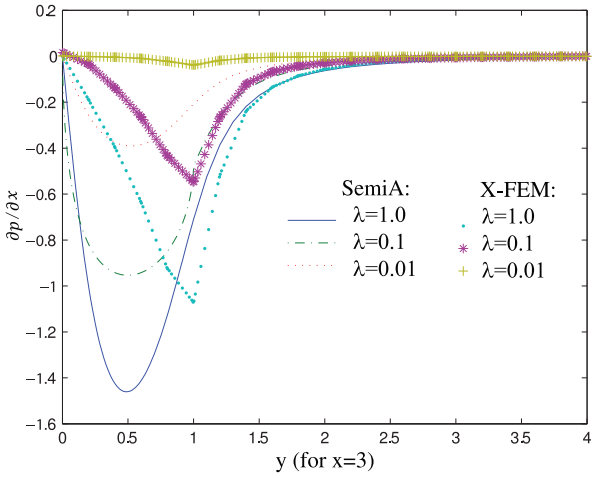


**Fig. 14.** Comparison of the semianalytical and XFEM solution. Variation of the pressure gradient component tangential to the crack, $\partial p/\partial x$, along the crack at $x = 3$ for different values of $\lambda$.

### 5.3. Permeability test

Transport properties of a porous media, such as the water absorption, capillary absorption, water penetration and water permeability coefficient, can be assessed by different tests that can be used to characterise the internal structure of a porous material. In this example we simulate the determination of the water permeability coefficient of a cement mortar specimen using the constant head test method. The test was carried out using cement mortar cylinders with a vertical slot placed in its centre. For the casting of the specimens, molds with diameter 100 mm and height 50 mm were used and X-Ray sheets were introduced during the molding to produce cracks with known value of the width. The X-Ray sheets had $T_h = 0.02$ mm thick and $H = 50$ mm height and four different widths $w_h$ were considered: 10 mm, 20 mm, 30 mm and 40 mm. To ensure that the flow was axial, the molded cylindrical specimens were painted with waterproof paint. The permeability test consisted in applying a low pressure at the upper face and in holding constant the hydraulic head. When flow reached the steady state conditions, the outflow through the sample was then regularly measured to compute a global permeability coefficient. We refer to [2] for a detailed description of the experimental setup. The model problem for the XFEM is shown in Fig. 15($b$). The geometrical domain was discretised using 456 quadrilateral finite elements with biquadratic shape interpolation functions for the displacement and bilinear shape functions for the pressure. The number of integration points in the enriched finite elements was taken equal to 100. The poroelastic properties of the cement mortar specimen are given in Table 3.

For the fluid flow inside the discontinuity, two values of the rugosity coefficient were used, $f = 1.05$ and $f = 1.65$, whereas the water dynamic viscosity was $\mu = 1 \cdot 10^{-7} Ns/cm^2$. With these data, the hydraulic conductivity of the crack was then computed

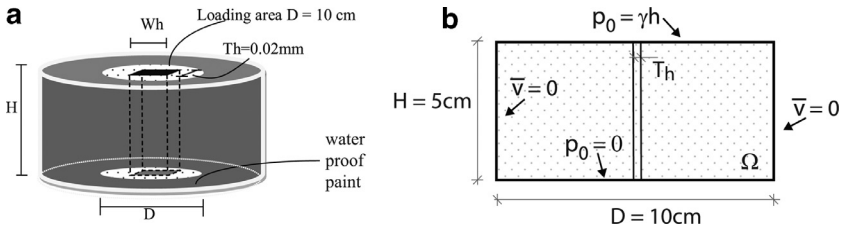


**Fig. 15.** Permeability test: (*a*) Experimental setup; (*b*) Geometry and boundary conditions of the model problem of Example 5.3.

**Table 3**
Poroelastic properties of the cement mortar specimen of Example 5.3.

| | |
|---|---|
| Young modulus, $E$ [GPa] | 11 |
| Poisson coefficient, $\nu$ | 0.2 |
| Water compressibility modulus, $K_f$ [GPa] | $1 \cdot 10^{18}$ |
| Biot's coefficient $\alpha$ | 1 |
| Bulk permeability coefficient, $k_f$ [cm/s] | $1 \cdot 10^{-10}$ |

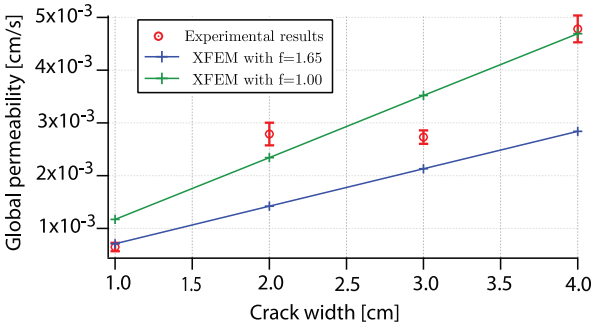


**Fig. 16.** Permeability test: comparison of the XFEM results and the experimental ones obtained for different crack widths as in [2].

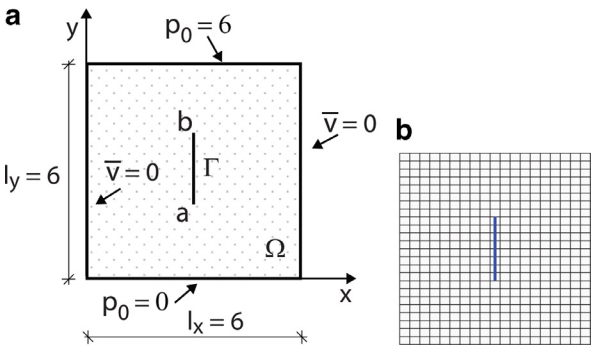


**Fig. 17.** (*a*) Geometry and boundary conditions of the model problem of Example 5.4. (*b*) Finite element mesh.

by means of the equation $k_d = 4h^2/(12f\mu)$ assuming the cubic law for fluid flow between two parallel plates [42] as discussed in Section 2.4.

As for the boundary conditions, the specimen was impermeable along the lateral surface, whereas drained conditions were assumed on the two basis, with the pressure on the upper face given by $p = \gamma h$ with $h = 30$ cm and $\gamma$ the unit weight of the water, whereas on the lower face $p = 0$. Fig. 16 displays the numerical results for the permeability coefficient as obtained by the XFEM, compared to the experimental ones obtained in [2]. One can appreciate generally a good agreement.

### 5.4. A fully coupled problem

In this example we study the model problem of Fig. 17 where we do not make anymore the assumption of steady-state flow conditions, so that we need to solve the fully coupled equations (3.9). An objective of this example is to analyze the effects of the

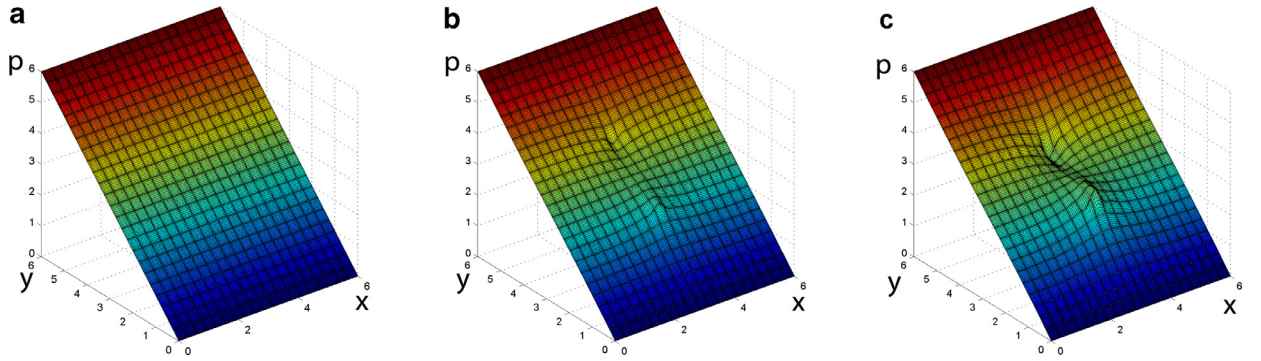


**Fig. 18.** Pressure field obtained by the XFEM solution for: (a) $\lambda = 0.01$, (b) $\lambda = 0.1$ and (c) $\lambda = 1$.

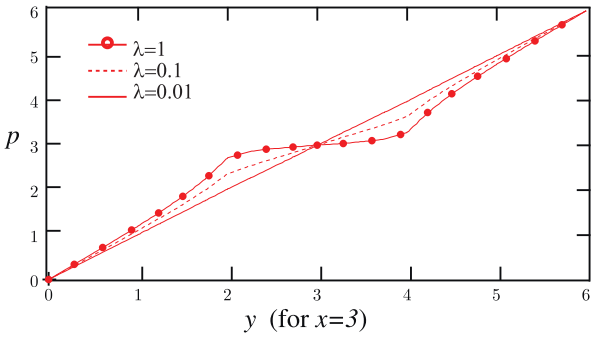


**Fig. 19.** XFEM solution. Variation of the pressure along the crack for different values of $\lambda$.

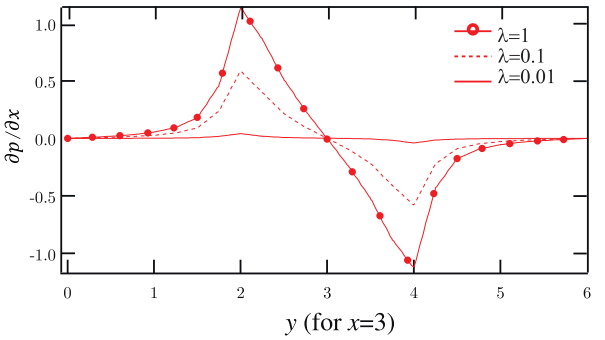


**Fig. 20.** Variation of $\partial p/\partial x$ along $x = 3$ for different values of $\lambda$.

flow on the opening of the crack for different values of $\lambda$, i.e. for different values of the ratio of permeability of the porous medium surrounding the crack and the permeability of the crack. The geometry of the problem is the same as the one considered in the Example 5.1, being different now the boundary conditions. These are given by the drained conditions on the edges $y = 0$ and $y = 6$ with constant value of the pressure equal to $p = 0$ and $p = 6$, respectively, impermeable lateral edges, and no prescribed condition is assigned on the interface $\Gamma$. The poroelastic material properties are the same as the one of Example 5.1 and are given in Table 1. The finite element mesh used for computing the XFEM solution is also the same as the one employed in the Example 5.1, taking here as well the same number of Gauss integration points in the enriched finite elements.

Fig. 18 (*a*), (*b*) and (*c*) show the pressure distribution calculated for different values of $\lambda$. Likewise the Example 5.2, also here we observe a different pressure distribution in the neighbourhood of the crack according to the value of $\lambda$. More specifically, for low values of $\lambda$, the pressure distribution seems not to be affected by the presence of the crack, whereas for higher values, although the flow is unidirectional and parallel to the direction of the crack, the pressure in the surrounding of the crack is modified. This behaviour can be better appreciated in Fig. 19, which displays the pressure distribution along the crack for different values of $\lambda$. So, for instance, we note that for $\lambda = 0.01$, i.e. for the case of a high permeable porous medium compared to the crack permeability, the pressure in the crack presents a hydrostatic like variation.

To analyse the changes on the fluid flow, we plot the variation of the components $\partial p/\partial x$ and $\partial p/\partial y$ of the pressure gradient in Fig. 20 and Fig. 21, respectively. In particular, Fig. 20 displays the variation of $\partial p/\partial x$, i.e. the normal flow to the crack, along the crack at $x = 3$. We observe that for a low value of $\lambda$, $\partial p/\partial x$ is zero and therefore there is no fluid that flows normal to the crack. If

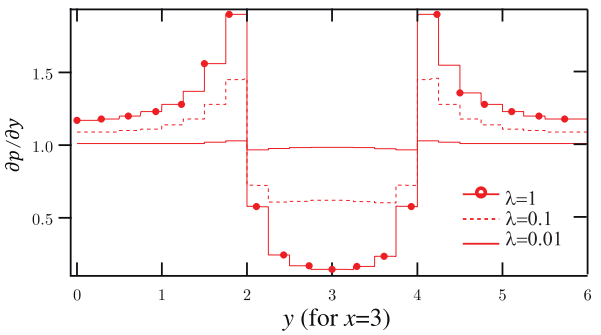


**Fig. 21.** Variation of $\partial p/\partial y$ along $x = 3$ for different values of $\lambda$.

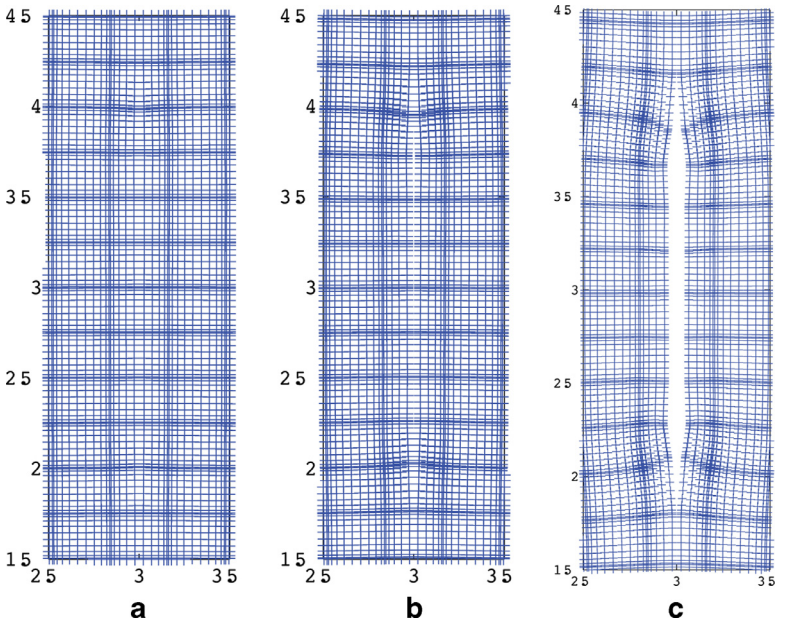


**Fig. 22.** Zooms showing the crack opening produced by the fluid flow for different values of $\lambda$: ($a$) COD $= 0.053$ mm for $\lambda = 0.01$, ($b$) COD $= 0.078$ mm for $\lambda = 0.1$ and ($c$) COD $= 0.207$ mm for $\lambda = 1$.

we increase the permeability, a normal component of flow appears. Fig. 21 shows the variation of $\partial p/\partial y$ along the crack as well. Here we observe that for low values of $\lambda$, $\partial p/\partial y$ is equal to one whereas for higher values of $\lambda$, the flow increases towards the two crack tips and presents the same sign and therefore same direction of flow. However, we note that the value of the flow decreases along the crack. This means that for higher values of $\lambda$, the flow along the crack is almost stopped and therefore the fluid leaves or enters normally to the crack. This behaviour also explains the major tendency that has the fluid to open the crack for higher values of $\lambda$. To confirm this fact, we display in Fig. 22 zooms of the crack region with the location of the Gauss points, where we can appreciate the higher values of the Crack Opening Displacement (COD) for higher values of $\lambda$. More precisely, we have that COD $= 0.053$ mm for $\lambda = 0.01$, COD $= 0.078$ mm for $\lambda = 0.1$ and COD $= 0.207$ mm for $\lambda = 1$.

To analyse finally the dependency of the results on the mesh discretisation, we plot in Fig. 23(a) and (b) the COD and the relative error with respect to the number of elements used in the XFEM computation for $\lambda = 1$, and assuming as reference values those associated with the XFEM solution obtained with the mesh of $79 \times 96$ elements. We observe that the COD assumes the value of $0.28\,mm$ with an accuracy of 5% with already few finite elements (value corresponding to the mesh of $19 \times 24$ elements). Table 4 reports then the CPU time with an Intel(R) Core(TM) i7-4510U CPU@2.00 GHz and 16 GB RAM and the COD for the different finite element meshes used in the computations for $\lambda = 1$, showing in general, that the computations are quite fast in $2D$.

## 6. Conclusions

In this paper we have proposed a numerical model of the hydromechanical behaviour of a porous linear elastic fractured medium which is built upon the XFEM and the reduced model of the fluid flow in thin cracks modelled individually. In the

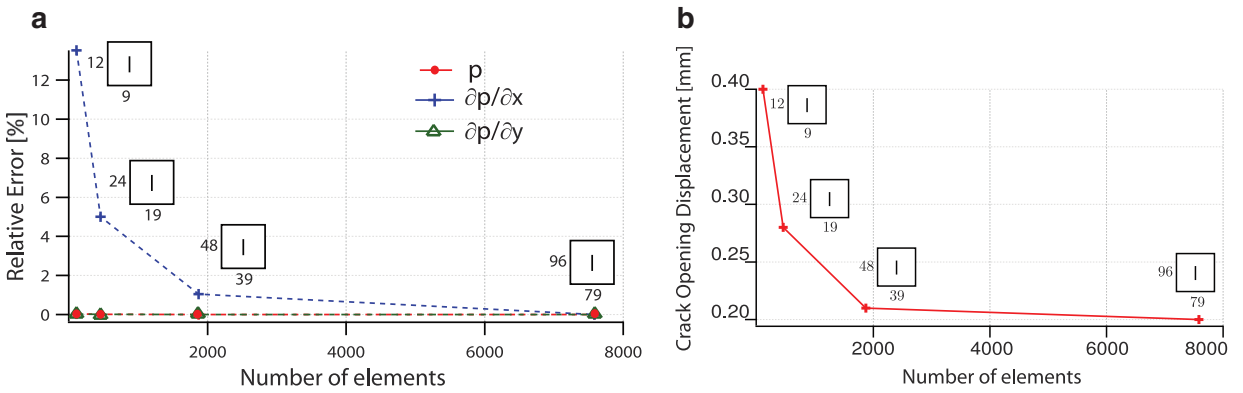


**Fig. 23.** XFEM results for $\lambda = 1$: (*a*) Relative error of the pressure and gradient of pressure for different number of finite elements; (*b*) Crack opening displacement for different number of finite elements.

**Table 4**
XFEM results for $\lambda = 1$: CPU time with an Intel Core i7-4510U@2.00 GHz and COD for different finite element meshes.

| $N_x \times N_y$ | Number of elements | Computation time [*s*] | COD [*mm*] |
|---|---|---|---|
| $9 \times 12$ | 108 | 7 | 0.40 |
| $19 \times 24$ | 456 | 17 | 0.28 |
| $39 \times 48$ | 1872 | 93 | 0.21 |
| $79 \times 96$ | 7584 | 1042 | 0.20 |

derivation of the model, two aspects have been specially taken into account. The first one is the setting of the interface boundary conditions obtained by assuming the cracks fully saturated and by averaging the Darcy law within the crack. The second one is the application of the XFEM for the space discretisation of the governing equations, due to the singularity of the displacement and pressure field.

To verify the XFEM solution, we have also developed a semianalytical model in the case of steady-state flow, given that in this case the governing equations decouple in the Laplace equation on a no-Lipschitz domain for the pressure, and in the linear elasticity equations for the effective stresses.

Four numerical examples have been presented. In the first two, which assume a steady-state fluid flow and different boundary conditions on the interface, we have observed in general a good agreement of the XFEM solution with the semianalytical one, though the XFEM solution was noted to underestimate the fluid flow in the porous media surrounding the crack and to give a much smoother transition. It is conjectured that this behaviour can be improved by modifying only the enrichment functions used for the pressure field approximation. In the third example, we have simulated the constant head test for finding the permeability coefficient of a cement mortar specimen with defined single cracks in its interior. We observed that the permeability coefficients computed using the XFEM results were agreeing quite well with the experimental ones, so that it can be stated that the XFEM model globally behaves well. Finally, we have considered a fully couple problem where we have analysed the flow in the porous media surrounding the crack as a function of the ratio of permeability of the porous media and of the crack, showing that for high permeability of the surrounding porous medium, the fluid tends to avoid the crack, whereas for low permeability of the surrounding porous medium, the fluid flows more rapidly in the crack and then along it, behaviour that was noted also in the analysis of the second example. For this last example, we have also computed the crack opening displacements for different values of $\lambda$ and assessed the quality of the XFEM solution with the number of finite elements employed in the computations.

## Acknowledgements

ML, JL, CT and AO gratefully acknowledge the partial financial support of the Argentinean Research Council, CONICET. ML and AO acknowledge the partial financial support of the Argentinean Agency through the Project Prestamo BID PICT PRH 30 N94 and the National University of Tucumán through the project PIUNT E527. The authors are also thankful to the anonymous referees for their critical comments that have lead to an improvement of the manuscript.

## Appendix A. Global matrices and load vectors

$$\boldsymbol{C} = \begin{bmatrix} 0 & 0 & 0 & \widehat{\boldsymbol{C}_{a1p1}} & \widehat{\boldsymbol{C}_{a1p2}} & \widehat{\boldsymbol{C}_{a1p3}} \\ 0 & 0 & 0 & \widehat{\boldsymbol{C}_{a2p1}} & \widehat{\boldsymbol{C}_{a2p2}} & \widehat{\boldsymbol{C}_{a2p3}} \\ 0 & 0 & 0 & \widehat{\boldsymbol{C}_{a3p1}} & \widehat{\boldsymbol{C}_{a3p2}} & \widehat{\boldsymbol{C}_{a3p3}} \\ \boldsymbol{C}_{p1a1} & \boldsymbol{C}_{p1a2} & \boldsymbol{C}_{p1a3} & \boldsymbol{C}_{p1p1} + \widehat{\boldsymbol{C}_{p1p1}} & \boldsymbol{C}_{p1p2} + \widehat{\boldsymbol{C}_{p1p2}} & \boldsymbol{C}_{p1p3} + \widehat{\boldsymbol{C}_{p1p3}} \\ \boldsymbol{C}_{p2a1} & \boldsymbol{C}_{p2a2} & \boldsymbol{C}_{p2a3} & \boldsymbol{C}_{p2p1} + \widehat{\boldsymbol{C}_{p2p1}} & \boldsymbol{C}_{p2p2} + \widehat{\boldsymbol{C}_{p2p2}} & \boldsymbol{C}_{p2p3} + \widehat{\boldsymbol{C}_{p2p3}} \\ \boldsymbol{C}_{p3a1} & \boldsymbol{C}_{p3a2} & \boldsymbol{C}_{p3a3} & \boldsymbol{C}_{p3p1} + \widehat{\boldsymbol{C}_{p3p1}} & \boldsymbol{C}_{p3p2} + \widehat{\boldsymbol{C}_{p3p2}} & \boldsymbol{C}_{p3p3} + \widehat{\boldsymbol{C}_{p3p3}} \end{bmatrix} \tag{A.1}$$

$$\boldsymbol{K} = \begin{bmatrix} \boldsymbol{K}_{a1a1} & \boldsymbol{K}_{a1a2} & \boldsymbol{K}_{a1a3} & \boldsymbol{K}_{a1p1} & \boldsymbol{K}_{a1p2} & \boldsymbol{K}_{a1p3} \\ \boldsymbol{K}_{a2a1} & \boldsymbol{K}_{a2a2} & \boldsymbol{K}_{a2a3} & \boldsymbol{K}_{a2p1} & \boldsymbol{K}_{a2p2} & \boldsymbol{K}_{a2p3} \\ \boldsymbol{K}_{a3a1} & \boldsymbol{K}_{a3a2} & \boldsymbol{K}_{a3a3} & \boldsymbol{K}_{a3p1} & \boldsymbol{K}_{a3p2} & \boldsymbol{K}_{a3p3} \\ 0 & 0 & 0 & \boldsymbol{K}_{p1p1} + \widehat{\boldsymbol{K}_{p1p1}} & \boldsymbol{K}_{p1p2} + \widehat{\boldsymbol{K}_{p1p2}} & \boldsymbol{K}_{p1p3} + \widehat{\boldsymbol{K}_{p1p3}} \\ 0 & 0 & 0 & \boldsymbol{K}_{p2p1} + \widehat{\boldsymbol{K}_{p2p1}} & \boldsymbol{K}_{p2p2} + \widehat{\boldsymbol{K}_{p2p2}} & \boldsymbol{K}_{p2p3} + \widehat{\boldsymbol{K}_{p2p3}} \\ 0 & 0 & 0 & \boldsymbol{K}_{p3p1} + \widehat{\boldsymbol{K}_{p3p1}} & \boldsymbol{K}_{p3p2} + \widehat{\boldsymbol{K}_{p3p2}} & \boldsymbol{K}_{p3p3} + \widehat{\boldsymbol{K}_{p3p3}} \end{bmatrix} \tag{A.2}$$

$$\boldsymbol{f} = \begin{bmatrix} \boldsymbol{f}_{a1} \\ \boldsymbol{f}_{a2} \\ \boldsymbol{f}_{a3} \\ f_{p1} \\ f_{p2} \\ f_{p3} \end{bmatrix} \tag{A.3}$$

where

$$\begin{aligned}
\boldsymbol{C}_{p(i)a(j)} &= -\int_\Omega \alpha \boldsymbol{N}_{p(i)}^T \boldsymbol{m}^T \boldsymbol{B}_{a(j)}\, \mathrm{d}V \\
\boldsymbol{C}_{p(i)p(j)} &= \int_\Omega K_f^{-1} \boldsymbol{N}_{p(i)}^T \boldsymbol{N}_{p(j)}\, \mathrm{d}V \\
\boldsymbol{K}_{a(i)a(j)} &= \int_\Omega \boldsymbol{B}_{a(i)}^T \boldsymbol{D} \boldsymbol{B}_{a(j)}\, \mathrm{d}V \\
\boldsymbol{K}_{a(i)p(j)} &= -\int_\Omega \alpha \boldsymbol{B}_{a(i)}^T \boldsymbol{m} \boldsymbol{N}_{p(j)}\, \mathrm{d}V \\
\boldsymbol{K}_{p(i)p(j)} &= -\int_\Omega k_f \boldsymbol{B}_{p(i)}^T \boldsymbol{B}_{p(j)}\, \mathrm{d}V \\
\widehat{\boldsymbol{C}_{a(i)p(j)}} &= -\int_\Gamma \boldsymbol{N}_{p(i)}^T\, 2h\, \boldsymbol{t}_\Gamma \cdot \langle \boldsymbol{B}_{a(j)} \rangle\, \mathrm{d}s - \int_\Gamma \boldsymbol{N}_{p(i)}^T [\![ \boldsymbol{B}_{a(j)} ]\!] \cdot \boldsymbol{n}_\Gamma\, \mathrm{d}s \\
\widehat{\boldsymbol{C}_{p(i)p(j)}} &= -\int_\Gamma \boldsymbol{N}_{p(i)}^T \frac{2h}{K_f} \boldsymbol{N}_{p(j)}\, \mathrm{d}s \\
\widehat{\boldsymbol{K}_{p(i)p(j)}} &= -\int_\Gamma \left( \boldsymbol{B}_{p(i)}^T \cdot \boldsymbol{t}_\Gamma^T \right) 2h\, k_d\, (\boldsymbol{t}_\Gamma \cdot \boldsymbol{N}_{p(j)})\, \mathrm{d}s \\
\boldsymbol{f}_{a(i)} &= \int_{\partial_t \Omega} \boldsymbol{N}_{a(i)}^T \bar{\boldsymbol{t}}\, \mathrm{d}s \\
f_{p(i)} &= \int_{\partial\Omega} \boldsymbol{N}_{p(i)}^T \bar{v}\, \mathrm{d}s,
\end{aligned} \tag{A.4}$$

with $i, j = 1, 2, 3$; $\boldsymbol{m} = (1,\ 1,\ 0)$; and $\boldsymbol{n}_\Gamma$ and $\boldsymbol{t}_\Gamma$ the unit normal and tangential vectors to the interface $\Gamma$, respectively.

## Appendix B. Mass balance in the discontinuity

The continuity equation of the fluid phase within the discontinuity $\Omega_c = ]-h, h[ \times \Gamma$ reads as

$$\int_\Gamma \int_{-h}^{h} \frac{\partial \rho_f}{\partial t} + \nabla \cdot (\rho_f \boldsymbol{v}_f)\, \mathrm{d}x^*\, \mathrm{d}y^* = 0. \tag{B.1}$$

Assuming that changes in the fluid mass inside the crack can be neglected, i.e. $\partial\rho_f/\partial t = 0$, and by applying the divergence theorem in Eq. (B.1) we obtain

$$0 = \int_\Gamma \int_{-h}^{h} \nabla\cdot(\rho_f \boldsymbol{v}_f)\,\mathrm{d}x^*\,\mathrm{d}y^* = \int_\Gamma \int_{-h}^{h} \rho_f\left(\frac{\partial v_{fx^*}}{\partial x^*} + \frac{\partial v_{fy^*}}{\partial y^*}\right)\mathrm{d}x^*\,\mathrm{d}y^*$$
$$= \int_\Gamma \int_{-h}^{h} \rho_f \frac{\partial v_{fx^*}}{\partial x^*} + \int_\Gamma \rho_f [\![ v_{fy^*} ]\!]\,\mathrm{d}x^*, \tag{B.2}$$

where $(v_{fx^*}, v_{fy^*})$ represent the components of $\boldsymbol{v}_f$ in the curvilinear reference system $(x^*, y^*)$, in which the domain $\Omega_c$ is represented.

Noting that

$$\int_\Gamma \int_{-h}^{h} \rho_f \frac{\partial v_{fx^*}}{\partial x^*}\,\mathrm{d}y^*\,\mathrm{d}x^* = \int_\Gamma \rho_f \frac{\partial}{\partial x^*}\int_{-h}^{h} v\,\mathrm{d}y^*\,\mathrm{d}x^* = \int_\Gamma \rho_f \frac{\partial q}{\partial x^*}\,\mathrm{d}x^*, \tag{B.3}$$

with $v_{fy^*} = \boldsymbol{v}_f\cdot\boldsymbol{n}_\Gamma$, the balance of mass inside the crack cavity $\Omega_c$ can be finally expressed as follows:

$$[\![ \boldsymbol{v}_f ]\!]\cdot\boldsymbol{n}_\Gamma + \frac{\partial q}{\partial x^*} = 0. \tag{B.4}$$

By taking the solid matrix incompressible, i.e. $\nabla\cdot\boldsymbol{v}_s = 0$, then there holds

$$n[\![ \boldsymbol{v}_f - \boldsymbol{v}_s ]\!]\cdot\boldsymbol{n}_\Gamma + \frac{\partial q}{\partial x^*} = 0 \tag{B.5}$$

thus

$$nk_f[\![ \nabla p ]\!]\cdot\boldsymbol{n}_\Gamma + \frac{\partial q}{\partial x^*} = 0, \tag{B.6}$$

where we have used the Darcy's law. From Eq. (4.2) and the representation (4.6), it is not difficult to show that

$$[\![ \nabla p(\hat{x}_0) ]\!]\cdot\boldsymbol{n}_{\Gamma 0} = 2\pi\phi(t_0), \tag{B.7}$$

which combined with (B.6) yields

$$\phi(t) = \frac{1}{2\pi k_f}\frac{\partial q}{\partial x^*}. \tag{B.8}$$

## References


[1] C.-M. Aldea, S.P. Shah, A. Karr, Permeability of cracked concrete, Mater. Struct. 32 (1999) 370–376.
[2] M.C. Torrijos, G. Giaccio, R. Zerbino, Internal cracking and transport properties in damaged concretes, Mater. Struct. 43 (2010) 109–121.
[3] J.R. Rice, M.P. Cleary, Some basic stress diffusion solutions for fluid-saturated elastic porous media with compressible constituents, Rev. Geophys. Space Phys. 14 (1976) 227–241.
[4] N.I. Muskhelishvili, Some Basic Problems in the Mathematical Theory of Elasticity, Noordhoff Ltd, Groningen- Netherlands, 1953.
[5] P.A. Liolios, G.E. Exadaktylos, A solution of steady-state fluid flow in multiply fractured isotropic porous media, Int. J. Solids Struct. 43 (2006) 3960–3982.
[6] F. Erdogan, G.D. Gupta, T.S. Cook, Numerical solution of singular integral equations, in: G.C. Sih (Ed.), Mechanics of Fracture, Vol. 1 Methods of Analysis and Solutions of Crack Problems, Noordhoff, Leyden, the Netherlands, 1973, pp. 368–425.Chap 7.
[7] A. Pouya, S. Ghabezloo, Flow around a crack in a porous matrix and related problems, Trans. Porous Media 84 (2010) 511–532.
[8] A. Pouya, Three–dimensional flow in fractured porous media: A potential solution based on singular integral equations, Adv. Water Res. 35 (2012) 30–40.
[9] R.E. Showalter, Diffusion in poro-elastic media, J. Math. Anal. Appl. 251 (2000) 310–340.
[10] T. Belytschko, T. Black, Elastic crack growth in finite elements with minimal remeshing, Int. J. Numer. Methods Eng. 45 (1999) 601–620.
[11] N. Moes, J. Dolbow, T. Belytschko, A finite element method for crack growth without remeshing, Int. J. Numer. Methods Eng. 46 (1999) 131–150.
[12] I. Babuska, J.M. Melenk, The partition of unity method, Int. J. Numer. Methods Eng. 40 (1997) 727–758.
[13] C.A. Duarte, J.T. Oden, H-p clouds – An h-p meshless method, Numer. Methods Part. Differ. Equ. 12 (1996) 673–705.
[14] R. de Borst, J. Rethore, M.-A. Abellan, A numerical approach for arbitrary cracks in a fluid–saturated medium, Arch. Appl Mech 75 (2006) 595–606.
[15] J. Rethore, R. de Borst, M.-A. Abellan, A two-scale approach for fluid flow in fractured porous media, Int. J. Numer. Meth. Engng 71 (2007) 780–800.
[16] R. de Borst, J. Rethore, M.-A. Abellan, A precis of two–scale approaches for fracture in porous media, in: R. de Borst, T. Sadowski (Eds.), Lecture Notes on Composite Materials: Solid Mechanics and its Applications, Springer Netherlands, 2009, pp. 149–171.
[17] F. Liu, L.-q. Zhao, P.-l. Liu, Z.-f. Luo, N.-y. Li, P.-s. Wang, An extended finite element method for fluid flow in fractured porous media. Math. Probl. Eng. Article ID 604212.
[18] A.R. Khoei, E. Haghighat, Extended finite element modeling of deformable porous media with arbitrary interfaces, Appl. Math. Modell. 35 (2011) 5426–5441.
[19] T. Mohammadnejad, A.R. Khoei, Hydro-mechanical modeling of cohesive crack propagation in multiphs porous media using the extended finite element method, Int. J. Numer. Anal. Methods Geomech. 10 (2013) 1247–1279.
[20] J. Adachi, E. Siebrits, A. Peirce, J. Desroches, Computer simulation of hydraulic fractures, Int. J. Rock Mech. Mining Sci. 44 (2007) 739–757.
[21] J. Desroches, E. Detournay, B. Lenoach, P. Papanastasiou, M. Thiercelin, A. Cheng, The crack tip region in hydraulic fracturing, Proc. Royal Soc. Lond. A 447 (1994) 39–48.
[22] M.J. Hunsweck, Y. Shen, A.J. Lew, A finite element approach to the simulation of hydraulic fractures with lag, Int. J. Numer. Anal. Methods Geomech. 37 (2013) 993–1015.
[23] B. Lecampion, An extended finite element method for hydraulic fracture problems, Commun. Numer. Methods Eng. 25 (2009) 121–133.
[24] J.B. Lucero, M. Luege, A. Orlando, M.C. Torrijos, XFEM modelling of hydraulic fracturing, in: Proceedings on the 1st Pan-American Congress on Computational Mechanics - España. Barcelona. CIMNE. 2015. 1st Pan-American Congress on Computational Mechanics, 2015.
[25] J. Chessa, T. Belytschko, An extended finite element method for two-phase fluids: flow simulation and modeling, J. of Appl. Mech. 70 (2003) 10–17.
[26] H.F. Wang, Theory of Linear Poroelasticity with Applications to Geomechanics and Hydrogeology, Princeton University Press, 2000.
[27] P. Angot, F. Boyer, F. Hubert, Asymptotic and numerical modelling of flows in fractured porous media, ESAIM: M2AN 43 (2009) 239–275.

[28] M. Lesinigo, C. D'Angelo, A. Quarteroni, A multiscale Darcy–Brinkman model for fluid flow in fractured porous media, Numer. Math. 117 (2011) 717–752.
[29] V. Martin, J. Jaffré, J.E. Roberts, Modelling fractures and barriers as interfaces for flow in porous media, SIAM J. Sci. Comput. 26 (2005) 1667–1691.
[30] M. Discacciati, A. Quarteroni, A. Valli, Robin–Robin domain decomposition methods for the Stokes–Darcy coupling, SIAM J. Numer. Anal. 45 (2007) 1246–1268.
[31] A.A. Hill, B. Straughan, Poiseuille flow in a fluid overlying a porous medium, J. Fluid Mech. 603 (2008) 137–149.
[32] F. dell'Isola, A. Madeo, P. Seppecher, Boundary conditions at fluid-permeable interfaces in porous media: A variational approach, Int. J. Solids Struct. 46 (2009) 3150–3164.
[33] T. Levy, E. Sanchez-Palencha, On boundary conditions for fluid flow in porous media, Int. J. Eng. Sci. 13 (1975) 923–940.
[34] D.A. Nield, The Beavers–Joseph boundary condition and related matters: A historical and critical note, Trans. Porous Media 78 (2009) 537–540.
[35] F.J. Vernerey, The effective permeability of cracks and interfaces in porous media, Trans. Porous Media 93 (2012) 815–829.
[36] Z. Li, K. Ito, The Immersed Interface Method: Numerical Solutions of PDEs Involving Interfaces and Irregular Domains, SIAM, Philadelphia, 2006.
[37] R. LeVeque, Z. Li, The immerse interface method for elliptic equations with discontinuous coefficients and singular sources, SIAM J. Numer. Anal. 31 (1994) 1019–1044.
[38] M.A. Biot, General theory of three-dimensional consolidation, J. Appl. Phys. 12 (1941) 155–164.
[39] O. Coussy, Mechanics and Physics of Porous Solids, Wiley, 2010.
[40] M. Chandesris, D. Jamet, Jump conditions and surface-excess quantities at a fluid/porous interface: A multi-scale approach, Trans. Porous Media 78 (2009) 419–438.
[41] R.W. Lewis, B.A. Schrefler, The Finite Element Method in the Static and Dynamic Deformation and Consolidation of Porous Media, 2nd Edition, John Wiley & Sons, 1999.
[42] P.A. Witherspoon, J.S. Wang, K. Iwai, J.E. Gale, Validity of cubic law for fluid flow in a deformable rock fracture, Water Res. Res. 16 (1980) 1016–1024.
[43] M. Chandesris, D. Jamet, Boundary conditions at a planar fluid-porous interface for a Poiseuille flow, Int. J. Heat Mass Trans. 49 (2006) 2137–2150.
[44] B. Goyeau, D. Lhuillier, D. Gobin, M.G. Velarde, Momentum transport at a fluid-porous interface, Int. J.Heat Mass Trans. 46 (2003) 4071–4081.